Draft version August 29, 2025
Typeset using LaTeX **twocolumn** style in AASTeX7.0.1

On the Regulation of the Solar Wind Helium Abundance by the Hydrogen Compressibility

B. L. Alterman[1] and Raffaella D'Amicis[2]

[1] *Heliophysics Science Division*
NASA Goddard Space Flight Center
8800 Greenbelt, RD
Greenbelt, MD 20771, USA
[2] *INAF - Institute for Space Astrophysics and Planetology*
Via Fosso del Cavaliere, 100
00133 Rome, Italy

(Received August 29, 2025)

Submitted to ApJ

ABSTRACT

Traditionally, fast solar wind is considered to originate in solar source regions that are continuously open to the heliosphere. In contrast, slow solar wind is considered to originate in source regions that are only intermittently open to the heliosphere. In fast wind, the gradient of the solar wind helium abundance ($A_{\rm He}$) with increasing solar wind speed ($v_{\rm sw}$) is approximately 0 and $A_{\rm He}$ is fixed at $\sim 50\%$ of the photospheric value. In slow wind, this gradient is large and $A_{\rm He}$ is highly variable and $A_{\rm He}$ doesn't exceed this $\sim 50\%$ value. Although the normalized cross helicity in fast wind is typically observed to approach 1, this is not universally true and Alterman & D'Amicis (2025) show that $\nabla_{v_{\rm sw}} A_{\rm He}$ in fast wind unexpectedly increases with decreasing $|\sigma_c|$. We show that these large $\nabla_{v_{\rm sw}} A_{\rm He}$ are due to the presence of compressive fluctuations in fast wind. Accounting for the solar wind's compressibility ($|\delta n_{\rm H}/n_{\rm H}|$), there exists two subsets of enhanced $A_{\rm He}$ in excess of typical fast wind values. The subset corresponding to large solar wind compressibility is likely from neither continuously nor intermittently open sources. The portion of the solar wind speed distribution over which these fluctuations are most significant corresponds to the range of Alfvén wave-poor solar wind from continuously open source regions, which is likely analogous to the Alfvénic slow wind. Mapping the results of this work to Alterman & D'Amicis (2025) and vice versa shows that, in any given $|\delta n_{\rm H}/n_{\rm H}|$ quantile, $|\sigma_c| \lesssim 0.65$, an upper bound on non-Alfvénic cross helicity. Similarly, $|\delta n_{\rm H}/n_{\rm H}| \lesssim 0.15$ in any given $|\sigma_c|$ quantile, an upper bound on incompressible solar wind fluctuations. We conclude that $|\delta n_{\rm H}/n_{\rm H}|$ is essential for characterizing the solar wind helium abundance and possibly regulating it.

Keywords: Solar wind (1534), Fast solar wind (1872), Slow solar wind (1873), Abundance ratios (11), Chemical abundances (224), Alfven waves (23), Magnetohydrodynamics (1964)

1. INTRODUCTION

Based on the bimodal distribution of speeds observed near Earth in the ecliptic plane during solar minima, the solar wind has be classified into fast and slow speeds. Fast wind is typically associated with sources on the Sun that are continuously open to the heliosphere and have radial magnetic field lines. Slow wind is typically tied to sources that are intermittently open to the heliosphere. Coronal holes (CHs) are the prototypical example of the former (Phillips et al. 1994; Geiss et al. 1995b). The latter include solar sources like helmet streamers, pseudostreamers, and the boundaries between pseudostreamers and CHs (Fisk et al. 1999; Subramanian et al. 2010; Antiochos et al. 2011; Crooker et al. 2012; Abbo et al. 2016; Antonucci et al. 2005). These intermittently open sources are also referred to as "magnetically closed". The differences between these sources lead to distinct *in situ* signatures. For example, fast

Corresponding author: B. L. Alterman
b.l.alterman@nasa.gov

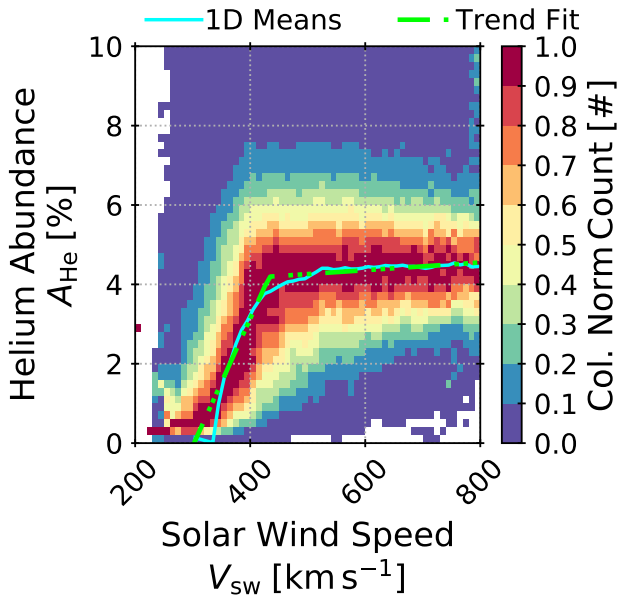

Figure 1. The helium abundance as a function of solar wind speed. $A_{\rm He}$ has been normalized to its maximum value in each column. The blue line indicates the mean value of $A_{\rm He}$ in each column. The dash-dotted green line is a bilinear fit to these means using Equation (2). The helium abundance monotonically increases from 0% to 4.19% in slow wind and saturates to this $A_{\rm He} = 4.19\%$ in fast solar wind for which $v_{\rm sw} > 433$ km s^{-1}.

solar wind from magnetically open regions displays enhanced helium- and heavy ion-to-hydrogen abundances (Alterman et al. 2024; Zurbuchen et al. 2016; Lepri et al. 2013; Pilleri et al. 2015) and temperature ratios (Kasper et al. 2008, 2017; Tracy et al. 2016; Stakhiv et al. 2016). The speed at which helium and heavy ions stream along the magnetic field in fast wind from magnetically open sources is also faster than the protons and constrained to a fraction of the Alfvén speed that depends on the ion species (Kasper et al. 2006; Stakhiv et al. 2016; Alterman et al. 2018; Berger et al. 2011; Klein et al. 2021; Verniero et al. 2020, 2022; Ďurovcová et al. 2019b). Moreover, the fast wind carries a chemical composition and charge-state ratios that are different from those observed in the slow wind, which reflects the differences in the magnetically open and closed topology of their sources (von Steiger et al. 2000; Geiss et al. 1995b,a; Zhao et al. 2017, 2022; Xu & Borovsky 2015; Fu et al. 2017, 2015; Brooks et al. 2015). Of these properties, Alterman & D'Amicis (2025) used the chemical composition and the Alfvénic content of solar wind fluctuations to statistically tie *in situ* observations to their solar source regions. We refer to Alterman & D'Amicis (2025) as Paper 1.

Type	Typical Abundance
Slow Wind[a]	1 - 5%
Fast Wind[b]	5%
ICMEs[c]	Highly variable, up to $> 10\%$
SIRs[d]	2-3% (Slow Wind) to 6-8% (Fast Wind)

[a] Aellig et al. (2001); Alterman & Kasper (2019); Alterman et al. (2021); Kasper et al. (2007); Alterman et al. (2025); Song et al. (2022); Alterman & D'Amicis (2025); Yogesh et al. (2021)
[b] Alterman & D'Amicis (2025); Alterman & D'Amicis (2025a); Yogesh et al. (2021); Song et al. (2022)
[c] Starkey et al. (2024); Khokhlachev et al. (2022); Song et al. (2022)
[d] Yogesh et al. (2023); Ďurovcová et al. (2019a)

Table 1. The typical helium abundance at L1 in different types of solar wind and transient events including ICMEs and stream interaction regions (SIRs).

In Paper 1, the chemical composition is characterized by the helium abundance, given by Equation (1)

$$A_{\rm He} = 100 \times \frac{n_{\rm He}}{n_{\rm H}} \tag{1}$$

where $n_{\rm H}$ and $n_{\rm He}$ are the ionized hydrogen and fully ionized helium number densities. Table 1 gives typical values for $A_{\rm He}$ in various types of solar wind and transient events. Figure 1 is a simplified version of Figure 3 in Paper 1, plotting $A_{\rm He}$ as a function of $v_{\rm sw}$. Here, the columns are normalized to their maximum values so that slow wind, which is observed in the ecliptic plane more frequently than fast wind, does not obscure the overall trend. Reducing the data in each column to a mean and standard deviation yields the solid blue line. Because this figure reproduces a result in Paper 1 the standard deviations, which fall at approximately the 0.6 color level, are omitted for visual clarity. The authors then fit the trend of these central values in each column to produce the bi-linear fit in the dash-dotted line. The bi-linear function is given by Equation (2)

$$A(v) = \min\left[m_1(v - v_1), m_2(v - v_2)\right] \tag{2}$$

where $A(v)$ is the abundance as a function of speed. The slopes and x-intercepts of the two lines are m_i and v_i for subscripts 1 and 2. Nominally, we consider line 1 to be the steeper gradient (slow wind). The speed at which the two lines intersect is

$$v_s = \frac{m_1 v_1 - m_2 v_2}{m_1 - m_2}. \tag{3}$$

The corresponding abundance is A_s.

Paper 1 identifies the point in the $(v_{\rm sw}, A_{\rm He})$-plane at which the gradient of $A_{\rm He}$ as a function of $v_{\rm sw}$ decreases as $(v_s, A_s) = \left(433\ {\rm km\,s^{-1}}, 4.19\%\right)$. $A_s = 4.19 \pm 0.05\%$ is

$49 \pm 2\%$ of the photospheric $A_{\rm He}$ (Asplund et al. 2021). At speeds $v_{\rm sw} < v_s$, the gradient of $A_{\rm He}$ as a function of $v_{\rm sw}$ ($\nabla_{v_{\rm sw}} A_{\rm He}$) is linear and strongly increasing. In contrast, $\nabla_{v_{\rm sw}} A_{\rm He}$ is close to zero at speeds $v_{\rm sw} > v_s$. Because this gradient is approximately flat at speeds $v_{\rm sw} > v_s$, the authors refer to this as the "saturation point". This change in the gradient statistically indicates the transition from slow to fast solar wind. We will refer to $(v_{\rm sw}, A_{\rm He}) < (v_s, A_s)$ as "below saturation" and $(v_{\rm sw}, A_{\rm He}) > (v_s, A_s)$ as "above saturation".

Paper 1 quantifies the Alfvénic content of the fluctuations with the normalized cross helicity (Tu & Marsch 1995; Bruno & Carbone 2013; Woodham et al. 2018)

$$\sigma_c = \frac{e^+ - e^-}{e^+ + e^-} \tag{4}$$

where the quantities on the right hand side $e^\pm = \frac{1}{2}\langle (z^\pm)^2 \rangle$ are the energies associated with the Elsässer variables. The Elsässer variables are given by the sum and difference of the velocity and magnetic field fluctuations in Alfvén units $\boldsymbol{z}^\pm = \boldsymbol{v} \pm \frac{1}{\sqrt{\mu_0 \rho}} \boldsymbol{b}$ for plasma velocity fluctuation $\boldsymbol{v}$, magnetic field fluctuation $\boldsymbol{b}$, and solar wind mass density ρ (Elsasser 1950; Tu et al. 1989; Grappin et al. 1991). We calculate these fluctuations as $X - \langle X \rangle$ where $\langle X \rangle$ is a 1hr rolling mean, a typical Alfvénic timescale at 1 AU (Tu et al. 1989; D'Amicis & Bruno 2015; D'Amicis et al. 2022). The normalized cross helicity approaches ± 1 as the dominant mode in a plasma observation is closer to a pure Alfvén mode. Typically, σ_c is a signed quantity where the sign indicates the direction (towards or away from the Sun) a given Alfvén wave propagates. However, this does not account for local rotations in the plasma associated, e.g., with switchbacks (McManus et al. 2020). As they are not concerned with the direction of the fluctuations, Paper 1 takes the absolute value.

The solar wind can be described as originating in an isothermal corona, evolving polytropically through the inner heliosphere, and in the case of fast wind, it continues to accelerate in transit due to forcing by Alfvén wave pressure gradients (Rivera et al. 2024). Alterman (2025) shows that, in the absence of Alfvén wave forcing, solar wind from continuously open source regions would only be accelerated to "intermediate" speeds for which the source region is ambiguous, not the fastest, non-transient speeds typical of fast wind. This suggests that the energy in the Alfvénic fluctuations at these intermediate speeds is less than the energy in the fluctuations carried in faster speed wind. We refer to this as "wave-poor" fast wind and it is likely synonymous with the Alfvénic slow wind (Marsch et al. 1981; D'Amicis et al. 2011). This suggests the Alfvénic content of the solar wind is essential for understanding its evolution through interplanetary space.

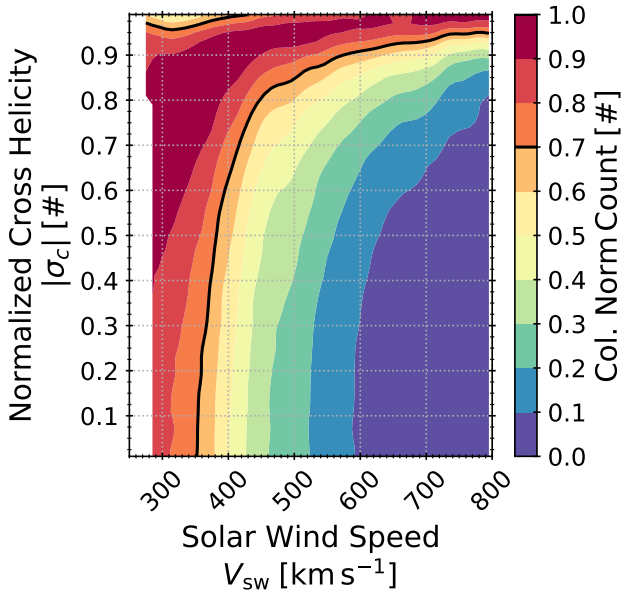

Figure 2. A contour plot of the PDF of $|\sigma_c|$. The columns in the underlying 2D histogram have been normalized to their maximum value. The contour at 0.7 is indicated in black.

Figure 2 is a contour plot of $|\sigma_c|$ ($v_{\rm sw}$) using Wind/FC observations from L1, recreating the relevant details from Figure 4 in Paper 1. For the same reason as in Figure 1, the columns in the underlying histogram have been normalized to their maximum value. These contours are smoothed with a 1σ Gaussian kernel for visual clarity. This figure shows that $|\sigma_c| \to 1$ as $v_{\rm sw}$ increases, indicating that the dominant wave mode observed in the solar wind is more likely to be Alfvénic as $v_{\rm sw}$ increases.

Paper 1 summarizes the observations that have characterized the observed *in situ* relationship between $A_{\rm He}$ and $v_{\rm sw}$ that relate these observations to source regions. Paper 1 also summarizes the *in situ* observations that relate $|\sigma_c|$ to source regions. Relevant to this work, $A_{\rm He}$ carries information about solar wind source regions based on processes that happen in the chromosphere and transition region (Lie-Svendsen et al. 2001; Lie-Svendsen et al. 2002; Endeve et al. 2005; Lie-Svendsen et al. 2003; Hansteen et al. 1997), below the solar wind's sonic critical point (r_c). In contrast, $|\sigma_c|$ carries information about solar wind source regions above r_c and below or near the Alfvén radius (r_A), above which the solar wind magnetically disconnects from the Sun in the sense that modifications of the magnetic field driven by motion on the Sun's surface, solar rotation, etc. can no longer propagate along a given field line to reach the plasma and modify its state. Combining the observations of $|\sigma_c|$,

$A_{\rm He}$, and $v_{\rm sw}$, Paper 1 analyze how the gradient of $A_{\rm He}$ as a function of $v_{\rm sw}$ and the saturation point change with increasing $|\sigma_c|$.

Repeating their analysis for 15 quantiles in $|\sigma_c|$, Paper 1 shows that the saturation speed (v_s) and abundance (A_s) are divided into three intervals of $|\sigma_c|$: *Low*, *Mid*, and *High*. Across these intervals, v_s decreases and A_s increases. In other words, $\min(v_s)$ associated with the most Alfvénic wind (highest $|\sigma_c|$) and largest A_s is less than $\max(v_s)$ in the least Alfvénic wind (lowest $|\sigma_c|$) with the smallest A_s.

Paper 1 also analyzes the gradients of $A_{\rm He}$ with $v_{\rm sw}$ above and below saturation. The authors show that $\nabla_{v_{\rm sw}} A_{\rm He}$ is independent of $|\sigma_c|$ for $v_{\rm sw} < v_s$, suggesting the process responsible for the highly variable $A_{\rm He}$ in solar wind from magnetically closed sources is independent of $|\sigma_c|$ and therefore independent of Alfvénic processes near the source region. Analogous analysis with ACE/SWICS (Alterman et al. 2024) reveals a similar trend in which the gradients of heavy ion abundances below their respective saturation speeds are also indistinguishable and the process responsible for their variability does not preferentially couple to any particular ion(s). In contrast, $\nabla_{v_{\rm sw}} A_{\rm He}$ increases with decreasing $|\sigma_c|$ for $v_{\rm sw} > v_s$, suggesting that the Alfvénic content of solar wind observed above saturation is inversely related to these gradients. However, Paper 1 leaves this difference in $\nabla_{v_{\rm sw}} A_{\rm He}$ above and below saturation unexplained.

In summary, Paper 1 makes the following observations.

1. $A_{\rm He}$ is set below r_c.
2. $A_{\rm He}$ is larger in solar wind originating in open sources than in solar wind originating in intermittently open sources.
3. $v_{\rm sw}$ increases during solar wind propagation above r_A.
4. The in-transit acceleration mechanisms depend on source region (Rivera et al. 2024, 2025).
5. v_s and A_s are anti-correlated across across $|\sigma_c|$.
6. $\nabla_{v_{\rm sw}} A_{\rm He}$ is independent of $|\sigma_c|$ at $v_{\rm sw} < v_s$ and increases with decreasing $|\sigma_c|$ for $v_{\rm sw} > v_s$.

Based on these observations, Paper 1 infers that the minimum speed of solar wind from continuously open sources is less than the maximum intermittently open source regions. Such an inference is consistent with the Alfvénic slow wind originating from the low speed extension of plasma that would otherwise be categorized as fast wind from coronal holes (D'Amicis & Bruno 2015; Wang 1994; Wang & Ko 2019; Panasenco et al. 2019, 2020; Panasenco & Velli 2013; Panasenco et al. 2019; Chitta et al. 2025).

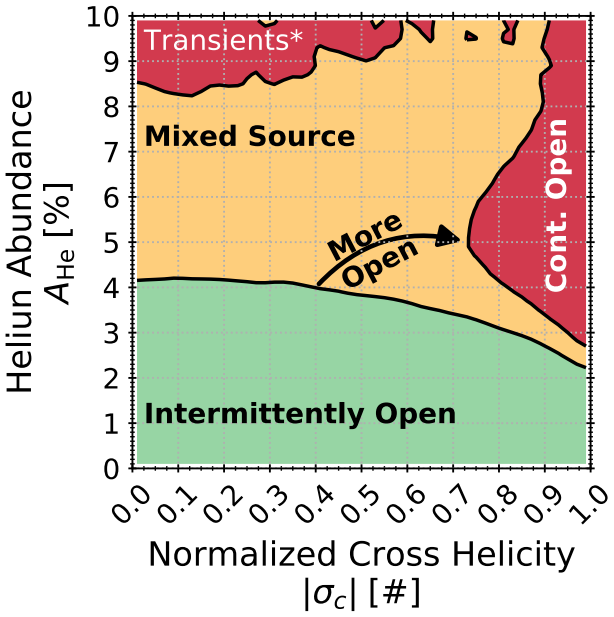

Figure 3. A plot of $v_{\rm sw}$ as a function of $|\sigma_c|$ and $A_{\rm He}$ with contours at $v_{\rm sw} = 300$ and 460 km s^{-1}. Paper 1 considers helium-poor solar wind with $A_{\rm He} < A_s$ to originate in intermittently open source regions and Alfvénic solar wind with $|\sigma_c| > 0.7$ in the red region to originate in continuously open source regions. That work hypothesizes that the speed enhancement of non-Alfvénic, helium rich solar wind in the top left corner of the plot is due to transients.

This analysis leads Paper 1 to propose that $v_{\rm sw}(|\sigma_c|, A_{\rm He})$ suggests a categorization scheme for solar wind observations at 1 AU. Figure 3 is a slightly modified version of their Figure 11 that illustrates it. There are two contours of $v_{\rm sw}$ plotted in the $(v_{\rm sw}, A_{\rm He})$-plane that separate the observations into four distinct regions. There is a helium-poor region without a preferred $|\sigma_c|$ across the bottom of the plane that Paper 1 suggests is solar wind from intermittently open sources. On the right side of the plane, there is an Alfvénic and helium rich region that Paper 1 suggests is solar wind from continuously open source regions. In the middle of the plane is a large region where solar wind observations from both sources mix across a narrow range of speeds. The range of $v_{\rm sw}$ in this region of the plane is consistent with the observed range of coronal mass ejection (CME) speeds (Webb & Howard 2012) and Paper 1 hypothesizes that the the speed enhancement in the top left corner is due to the presence of transients (Good et al. 2022; Yogesh et al. 2022; Song et al. 2022; Scolini et al. 2024). A detailed analysis of this is the subject of on going work. The authors then use this information to characterize significant processes in different regions

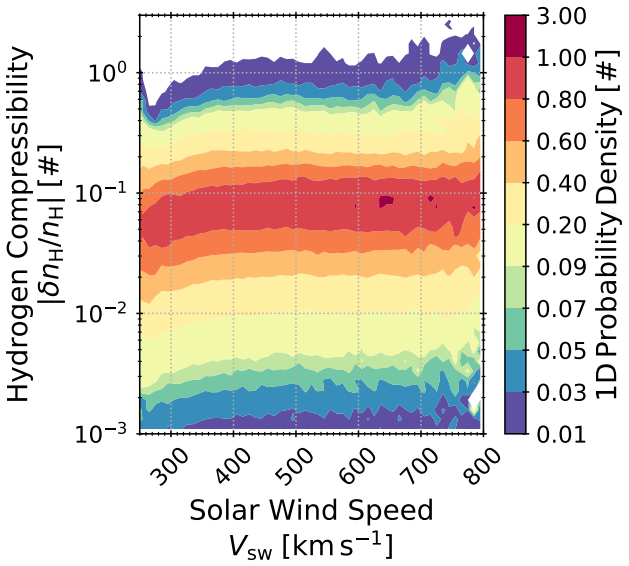

Figure 4. A contour plot of the PDF of $|\delta n_H/n_H|\,(v_{sw})$. In the underlying 2D histogram, the frequency of observing $|\delta n_H/n_H|$ in each column is normalized to its maximum value. The contours are smoothed with a 1σ Gaussian kernel for visual clarity.

of the distribution of solar wind speeds observed near Earth during solar minima.

In Alfvénic fluctuations, by definition, $\delta|\boldsymbol{B}|$ and δn tend towards zero. This is often referred to as "weak compressibility" (Bruno et al. 2001; Matteini et al. 2015). Intuitively, one expects that compressibility would decrease with v_{sw} given $|\sigma_c|$ increases with it. The solar wind's compressibility can be calculated from time series observations collected by a single spacecraft as

$$\left|\frac{\delta n_H}{n_H}\right| = \left|\frac{n_H - \langle n_H\rangle}{n_H}\right| \tag{5}$$

where n_H is the instantaneous hydrogen density and $\langle n_H\rangle$ is a rolling mean. The fluctuations δn_H are normalized to the observed n_H to quantify the amplitude of these fluctuations with respect to the observed density. We calculate $\langle n_H\rangle$ on the same 1hr time scale used for calculating σ_c and take the absolute value because we are concerned with the magnitude of the fluctuations. Compressive fluctuations, which can be defined as $|\delta n_H/n_H| > 0.1$ (Tu & Marsch 1994; Cuesta et al. 2023), are most common in non-Alfvénic solar wind.

Figure 4 is a contour plot of the PDF of $|\delta n_H/n_H|\,(v_{sw})$ using Wind/FC observations. As in Figure 2, the frequency of observation in each column in the underlying 2D histograms has been normalized to its maximum value and contours are smoothed with a 1σ Gaussian kernel for visual clarity. Figures 2 and 4 show that, although compressive fluctuations ($|\delta n_H/n_H| > 0.1$) are less common than non-compressive fluctuations ($|\delta n_H/n_H| < 0.1$), they are present across all v_{sw} and $|\sigma_c|$. Figure 5 is a contour plot of $|\delta n_H/n_H|\,(v_{sw}, |\sigma_c|)$. We calculate the average $|\delta n_H/n_H|$ as the logarithmic mean. It has been smoothed with a 1σ Gaussian kernel for visual clarity. The solid black line indicates $|\delta n_H/n_H| = 0.1$. The solid purple line indicates the 0.7 contour from Figure 2, indicating that $|\sigma_c|$ tends towards 1 as v_{sw} increases above $v_{sw} > 433$ km s^{-1}. This figure shows that, at these speeds, even as $|\sigma_c| \to 1$, compressive fluctuations occupy a significant fraction of plane and that compressive fluctuations become significant at high speeds with low cross helicity. In other words, the intuitive anti-correlation between $|\delta n_H/n_H|$ and $|\sigma_c|$ is most prominent at high speeds and virtually absent at low speeds. This work shows that the absence of the anti-correlation between $|\delta n_H/n_H|$ and $|\sigma_c|$ at lower speeds is likely is because the range of v_{sw} that correspond to incompressible, Alfvénic solar wind overlaps with the range corresponding to compressible, non-Alfvénic solar wind.

Compressive fluctuations are associated with slow modes and pressure balanced structures (PBS). Under magnetohydrodynamics (MHD), these two phenomena can be considered as different limits that both lead to $k_\perp/k_\parallel \to \infty$ (Hollweg et al. 2014). PBS can be described as the $k_\parallel \to 0$ limit, leading to structures in which the total thermal plus magnetic pressure is constant and that are convected along with the solar wind (Tu & Marsch 1994; Bruno & Carbone 2013). Although the total thermal plus magnetic pressure is constant in PBS, both quantities can fluctuate (Bruno & Carbone 2013; Tu & Marsch 1994; Marsch & Tu 1990) and the fluctuations in temperature likely maintain the pressure balance (Tu & Marsch 1994). Marsch & Tu (1990) argue these convected structures are related to the source of the solar wind. Specifically, Bruno & Carbone (2013) suggest that they are, "related to the fine ray-like structures or plumes associated with the underlying chromospheric network and interpreted as signatures of the interplanetary flowtubes." The more recently identified periodic density structures (PDS) may be related to these PBS (Kepko et al. 2024; Viall & Vourlidas 2015; Viall et al. 2009).

Slow mode waves can be derived as the $k_\perp \to \infty$ limit while $k_\parallel \to \infty$ is held finite (Hollweg et al. 2014). The are more difficult to study than PBS because they are typically Landau damped (Vasquez & Hollweg 1999; Cuesta et al. 2023). MHD predictions for slow mode waves agree with solar wind observations better than their kinetic counterparts (Verscharen et al. 2017) and compressive fluctuations may help maintain the stabil-

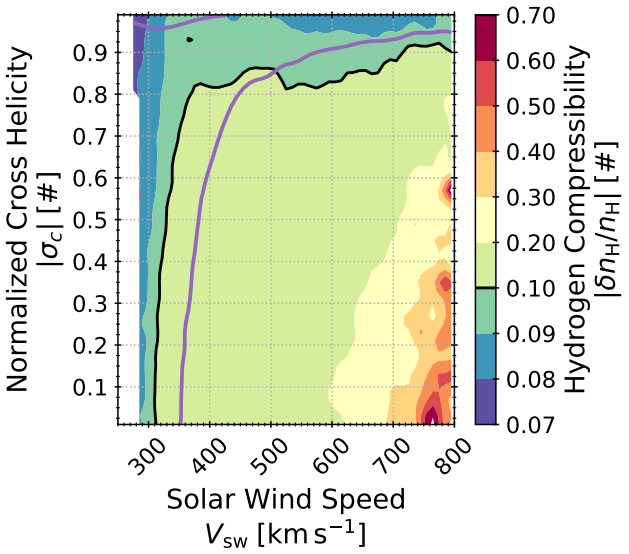

Figure 5. A contour plot of the PDF of $|\delta n_H/n_H|\,(v_{sw}, |\sigma_c|)$. Average $|\delta n_H/n_H|$ is calculated as the logarithmic mean. Contours are smoothed with a 1σ Gaussian kernel for visual clarity. The purple line is the 0.7 contour from Figure 2.

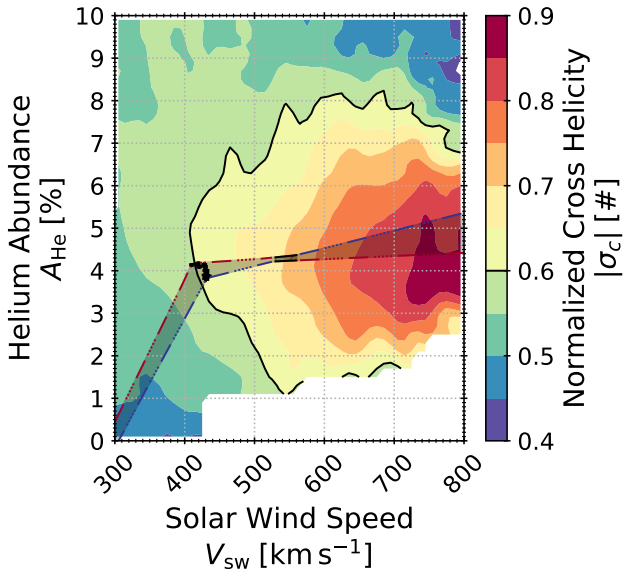

Figure 6. A contour plot of the normalized cross helicity as a function of solar wind speed and helium abundance. The contours are smoothed with a 1σ gaussian filter for clarity. The contour at $|\sigma_c| = 0.6$ is highlighted in black. The black points mark the saturation point (v_s, A_s). The saturation points occur at $|\sigma_c| > 0.6$. The shaded black region corresponds to fits to $A_{He}\,(v_{sw})$ for each $|\sigma_c|$ quantile: the red dash-dotted line is the high $|\sigma_c|$ edge and the blue dash–dotted line is the low $|\sigma_c|$ edge. The region from 530 to 560 km s^{-1} is where the maximum and minimum $|\sigma_c|$ fits to $A_{He}\,(|\sigma_c|)$ cross. This region is bounded by solid black lines and crosses the $|\sigma_c| = 0.7$ contour.

ity of fully ionized helium that is differentially streaming along the magnetic field faster than ionized hydrogen (Zhu et al. 2023). Using Parker Solar Probe (Probe) observations below 139.64 R_S, Adhikari et al. (2020) show that the solar wind compressibility stays roughly between 0.1 and 0.2 and is consistent with nearly incompressible MHD (NI-MHD). NI-MHD is an extension of MHD in which compressible fluctuations are generated by the nonlinear interaction between Alfvén waves propagating along the mean magnetic field and incompressible fluctuations propagating perpendicular to it (Zank & Matthaeus 1992).

In this paper, we analyze the increase of $\nabla_{v_{sw}} A_{He}$ with decreasing $|\sigma_c|$ for solar wind with speeds $v_{sw} > v_s$, which is unexplained in Paper 1. We show that they are related to the solar wind's compressibility. We also show that there are two distinct populations of enhanced $A_{He} > A_s$, one Alfvénic and one compressible, and infer that the compressible subset with enhanced $A_{He} > A_s$ is from neither of the traditional sources of solar wind that are intermittently or continuously open to the heliosphere. Mapping the results of this work to Alterman & D'Amicis (2025) and vice versa shows that, in any given $|\delta n_H/n_H|$ quantile, $|\sigma_c| \lesssim 0.65$, an upper bound on non-Alfvénic cross helicity. Similarly, $|\delta n_H/n_H| \lesssim 0.15$ in any given $|\sigma_c|$ quantile, an upper bound on incompressible solar wind fluctuations. We conclude that the hydrogen compressibility is essential for characterizing and possibly regulating the solar wind helium abundance.

2. OBSERVATIONS

We use solar wind measurements provided by the Wind Solar Wind Experiment (SWE) Faraday cups (FCs) (Ogilvie et al. 1995) and Magnetic field Investigation (MFI, Lepping et al. 1995; Koval & Szabo 2013). Our data selection follows Paper 1.

3. ANALYSIS

3.1. *Combining the Solar Wind Speed (v_{sw}), Helium Abundance (A_{He}), and Normalized Cross Helicity ($|\sigma_c|$)*

We begin with a semi-qualitative characterization of the relationship between $|\sigma_c|$, A_{He}, and v_{sw}. Figure 6 plots the former as a function of the other two. The contours are smoothed with a 1σ Gaussian filter for visual clarity. The white area in the bottom right is where the contours are sufficiently noisy that the smoothing fails. The contour at $|\sigma_c| = 0.6$ is highlighted with a thick black line. The dash-dotted lines are fits to $A_{He}\,(v_{sw})$ in 15 quantiles of $|\sigma_c|$ derived in Paper 1, Figure 4. The corresponding saturation points (v_s, A_s) across all

15 $|\sigma_c|$ quantiles are plotted in black and are located at $|\sigma_c| \gtrsim 0.6$, just beyond the highlighted contour. In Paper 1 the saturation speed (v_s) and saturation abundance (A_s) are each divided into *Low*, *Mid*, and *High* ranges. The three v_s and three A_s ranges are not identical.

Overall, $|\sigma_c|$ increases with increasing v_{sw}. For $v_{sw} \gtrsim v_s$, this increase becomes increasingly independent of A_{He}, especially for $A_{He} = 4.19\%$. Visually inspecting the underlying 2D histogram, we have qualitatively determined by eye that the slope of these contours larger and smaller than $A_{He} = 4.19\%$ are roughly symmetric with values of $\pm 3\%/200$ km s^{-1}, and are independent of $|\sigma_c|$. These slopes are not shown for visual clarity. In other words, at A_{He} larger and smaller than 4.19%, a larger v_{sw} is required to observe an increase in $|\sigma_c|$ and, as v_{sw} and $|\sigma_c|$ increase, the range of A_{He} on which higher $|\sigma_c|$ are observed decreases.

The fits of $A_{He}(v_{sw})$ for each $|\sigma_c|$ quantile are derived and originally presented in Paper 1, Figures 4 and 5. Figure 6 plots these fits as a black shaded region with the lines corresponding to the lowest (blue) and highest (red) $|\sigma_c|$ plotted as dash-dotted lines. For $v_{sw} > v_s$, the of $A_{He}(v_{sw})$ for low $|\sigma_c|$ becomes larger than the $A_{He}(v_{sw})$ fits for high $|\sigma_c|$ solar wind over the range of speeds 530 km s^{-1} $< v_{sw} <$ 560. This range of speeds corresponds to the region of Figure 6 in which the average $|\sigma_c|$ crosses the 0.7 contour, which Paper 1 shows, corresponding to the $|\sigma_c|$ in the non-Alfvénic subset as identified with A_s and in which A_s reaches its largest value. Over this 30 km s^{-1} range, the blue and red dash-dotted lines are replaced with solid black lines. This suggests the paradox that A_{He} in non-Alfvénic solar wind is greater than A_{He} in Alfvénic solar wind in the region of the plane where the solar wind is, on average, Alfvénic.

3.2. v_{sw}, A_{He}, and the Solar Wind Compressibility ($|\delta n_H/n_H|$)

Figures 4 & 5 of Paper 1 show that $\nabla_{v_{sw}} A_{He}$ for speeds $v_{sw} > v_s$ increases with decreasing $|\sigma_c|$. Figure 6 shows that $|\sigma_c|$ decreases for increasing A_{He} smaller and larger than $A_{He} = A_s$ and slower wind. Figure 7 shows contour plots of the $|\delta n_H/n_H|$ as a function of v_{sw} and A_{He}. Again, contours are smoothed with a 1σ filter for clarity. The solid black lines are the 1D fits of Gaussians to A_{He} PDFs in each v_{sw} column: the central line is the mean from the fit; the upper and lower lines indicate the corresponding 1σ widths. The contour at $|\delta n_H/n_H| = 0.09$ is at the boundary between yellow and blue; the $|\delta n_H/n_H| = 0.085$ contour is between the two lightest blue regions. The saturation points and fits to $A_{He}(v_{sw})$ are plotted in the same manner as Figure 6.

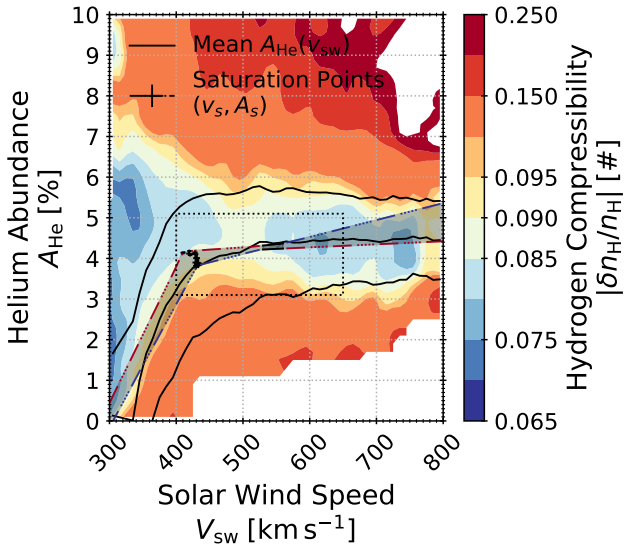

Figure 7. A contour plot of the compressibility as a function of solar wind speed and helium abundance. Contours are smoothed with a 1σ gaussian filter for clarity. Solid black lines are the mean and standard deviations from 1D fits plotted in Paper 1, Fig. 2. The shaded black region bounded by red and blue dash-dotted lines matches Figure 6. The region encircled by the box highlights the location of the saturation points (v_s, A_s) and is plotted in Figure 8.

The black dotted rectangle indicates the region enlarged in Figure 8. For speeds $v_{sw} > v_s$, low compressibility $|\delta n_H/n_H| \lesssim 0.09$ is roughly limited to a band in A_{He} that is narrower than the solid black lines corresponding to the 1σ fits to distributions of A_{He} in each v_{sw} bin.

Figure 8 enlarges the region surrounding the saturation point (v_s, A_s) and the crossover between $A_{He}(v_{sw})$ at $v_{sw} > v_s$ for low and high $|\sigma_c|$ in Figure 7. Several observations stand out:

1. A significant fraction of these saturation points are confined to the light blue region in which $|\delta n_H/n_H| = 0.085$ to 0.090 and $A_s \geq 4\%$, which corresponds to the *Mid* and *High* ranges of A_s defined in Paper 1.
2. The contour of $|\delta n_H/n_H| = 0.09$ changes at approximately $(A_s, v_{sw}) = (4\%, 400\ \text{km s}^{-1})$. For lower speeds, this contour of constant $|\delta n_H/n_H|$ follows increasing A_{He} and v_{sw}. At higher speeds, this contour is independent of A_s and follows increasing v_{sw} and then follows decreasing A_s as v_{sw} increases above $v_{sw} \approx 515$ km s^{-1}.
3. There are two regions corresponding to $|\delta n_H/n_H| \leq 0.085$, one corresponding to $v_{sw} \lesssim 470$ km s^{-1} and the other corresponding to $v_{sw} \gtrsim 530$ km s^{-1}. The region where $A_{He}(v_{sw})$

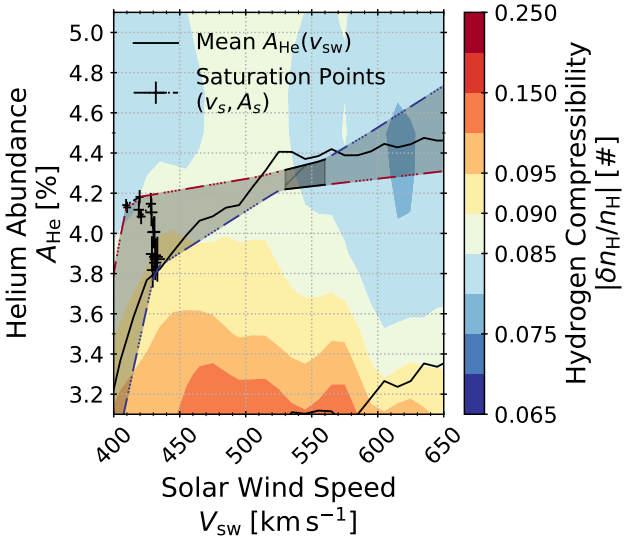

Figure 8. A zoom in of the region indicated in Figure 7. The gradient of the contour for $|\delta n_H/n_H| = 0.09$ changes across the saturation points. The fits $A_{He}(v_{sw})$ cross over the speed range $v_{sw} \approx 530$ to 560 km s^{-1}, which is bounded by solid black lines instead of red and blue dash-dotted lines. This region where the $A_{He}(v_{sw})$ fits at low $|\sigma_c|$ become larger than the fits at high $|\sigma_c|$ crosses the $|\delta n_H/n_H| = 0.085$ contour.

for low $|\sigma_c|$ becomes larger than $A_{He}(v_{sw})$ for high $|\sigma_c|$ begins at $v_{sw} = 530$ km s^{-1} and crosses this $|\delta n_H/n_H| = 0.085$ contour. The location of this intersection between the crossover region and $|\delta n_H/n_H| = 0.085$ is also where $|\sigma_c|(A_{He}, v_{sw}) = 0.7$ in Figure 6.

4. The contour $|\delta n_H/n_H| = 0.09$ traces out an increase in both A_{He} and v_{sw} for $v_{sw} < v_s$. For $v_{sw} > v_s$, the $|\delta n_H/n_H| = 0.09$ contour traces out constant or very slowly decreasing values of A_{He} with increasing v_{sw}.

These observations suggest that, in addition to A_{He}'s dependence on v_{sw} and $|\sigma_c|$, it also depends on $|\delta n_H/n_H|$ and that $|\delta n_H/n_H|$ may cross a value separating compressible and incompressible fluctuations in a region of the (v_{sw}, A_{He})-plane that Figure 6 shows the apparent paradox described above.

3.3. *Saturation Fits*

To characterize how the change in gradient $\nabla_{v_{sw}} A_{He}$ depends on the compressibility $|\delta n_H/n_H|$, we apply Paper 1's bilinear fitting method and repeat the analysis of Figure 1 for 15 quantiles of $|\delta n_H/n_H|$. Figure 9 plots the resulting fits of $A_{He}(v_{sw})$ in each $|\delta n_H/n_H|$ quantile, which is indicated by the color bar. In Paper 1, Figure 4 is the equivalent analysis for 15 quantiles in $|\sigma_c|$.

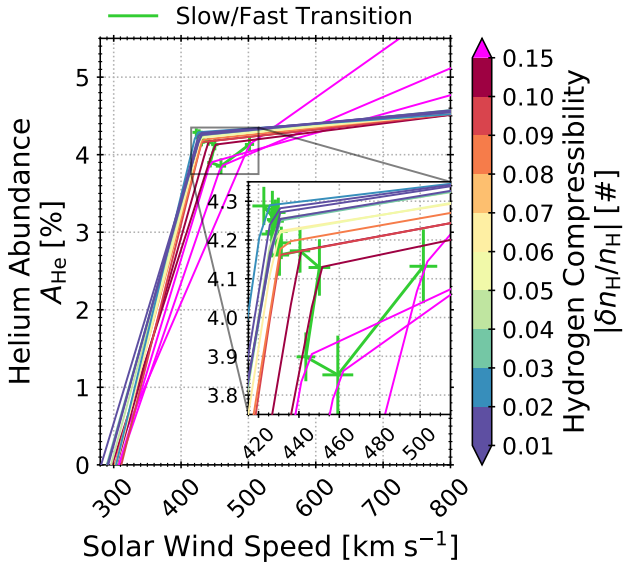

Figure 9. Fits of $A_{He}(v_{sw})$ for 15 quantiles of hydrogen compressibility ($|\delta n_H/n_H|$). The color bar identifies $|\delta n_H/n_H|$. Quantiles with $|\delta n_H/n_H| > 0.15$ are indicated in pink. The green plots indicate the saturation points (v_s, A_s).

Table 2 summarizes these saturation points. Quantiles corresponding to $|\delta n_H/n_H| > 0.15$ are plotted in pink. The green line plots the saturation points (v_s, A_s), connected in $|\delta n_H/n_H|$ order. The insert zooms in to the region immediately surrounding the saturation points. Broadly, there are two groups of quantiles: an incompressible subset ($|\delta n_H/n_H| < 0.15$) and a compressible subset ($|\delta n_H/n_H| > 0.15$). Below the saturation point – i.e. with $(v_{sw}, A_{He}) < (v_s, A_s) - \nabla_{v_{sw}} A_{He}$ is roughly consistent across all $|\delta n_H/n_H|$ quantiles. Above the saturation point – i.e. with $(v_{sw}, A_{He}) > (v_s, A_s) - \nabla_{v_{sw}} A_{He}$ is several times larger for the compressible quantiles (pink lines) than for the incompressible quantiles.

Figure 10 highlights the difference in $\nabla_{v_{sw}} A_{He}$ above and below the saturation point by scaling the fits in Figure 9 to their (v_s, A_s), which are plotted in green. Figure 5 in Paper 1 is the equivalent analysis for 15 quantiles in $|\sigma_c|$. This figure shows that the $\nabla_{v_{sw}} A_{He}$ are nearly indistinguishable below the saturation points. Above the saturation point, fits from the incompressible quantiles occupy a very narrow region. In contrast, $\nabla_{v_{sw}} A_{He}$ above the saturation points are similar when $|\delta n_H/n_H| < 0.15$ and markedly larger when $|\delta n_H/n_H| > 0.15$.

The insert in Figure 9 shows that, similar to the gradients $\nabla_{v_{sw}} A_{He}$, the saturation points (v_s, A_s) themselves also fall into incompressible and compressible subsets.

$\lvert\delta n_H/n_H\rvert$	Saturation Speed v_s $[\mathrm{km\,s^{-1}}]$	Saturation Abundance A_s [%]	Saturation Slope m_s $[10^{-3}\,\%\mathrm{km^{-1}\,s}]$	Vanishing Speed v_0 $[\mathrm{km\,s^{-1}}]$
0.003	430 ± 4	4.27 ± 0.04	0.8 ± 0.2	281 ± 8
0.012	427 ± 4	4.28 ± 0.05	0.7 ± 0.2	292 ± 4
0.020	428 ± 4	4.25 ± 0.05	0.9 ± 0.2	291 ± 4
0.028	423 ± 6	4.29 ± 0.05	0.6 ± 0.2	303 ± 9
0.037	429 ± 4	4.25 ± 0.05	0.9 ± 0.2	290 ± 4
0.046	428 ± 4	4.25 ± 0.04	0.8 ± 0.2	296 ± 4
0.057	427 ± 5	4.22 ± 0.06	0.9 ± 0.3	303 ± 10
0.068	429 ± 5	4.22 ± 0.06	0.8 ± 0.3	304 ± 10
0.082	431 ± 5	4.19 ± 0.04	0.9 ± 0.2	302 ± 8
0.098	430 ± 5	4.16 ± 0.05	1.0 ± 0.2	311 ± 6
0.117	441 ± 5	4.17 ± 0.06	1.0 ± 0.2	304 ± 8
0.143	450 ± 5	4.13 ± 0.07	1.1 ± 0.3	298 ± 5
0.182	443 ± 5	3.9 ± 0.06	2.4 ± 0.3	308 ± 5
0.252	459 ± 8	3.85 ± 0.1	3.7 ± 0.5	308 ± 12
0.649	502 ± 7	4.13 ± 0.1	6.1 ± 0.5	296 ± 5
0.085	428 ± 1	4.25 ± 0.02	0.81 ± 0.07	293 ± 2
0.1	428 ± 1	4.24 ± 0.02	0.82 ± 0.06	295 ± 2
0.15	430 ± 1	4.23 ± 0.01	0.84 ± 0.06	296 ± 2
Comp.	458 ± 3	4.00 ± 0.04	2.7 ± 0.2	301 ± 3

Table 2. Saturation points and slopes in Figures 11 and 12. We also include the speed v_0 at which the slow wind portion of the fit ($v_{sw} < v_s$) intersects the x-axis to completeness. From left to right, first four columns are v_s (Figure 11 (a)), A_s (Figure 11 (b)), saturation slope (Figure 12), and v_0 in $|\delta n_H/n_H|$ quantiles. The bottom four rows correspond to weighted averages taken across the incompressible subsets $|\delta n_H/n_H| < 0.085$, 0.1, and 0.15 along with the compressible subset $|\delta n_H/n_H| > 0.15$ under *Comp.*

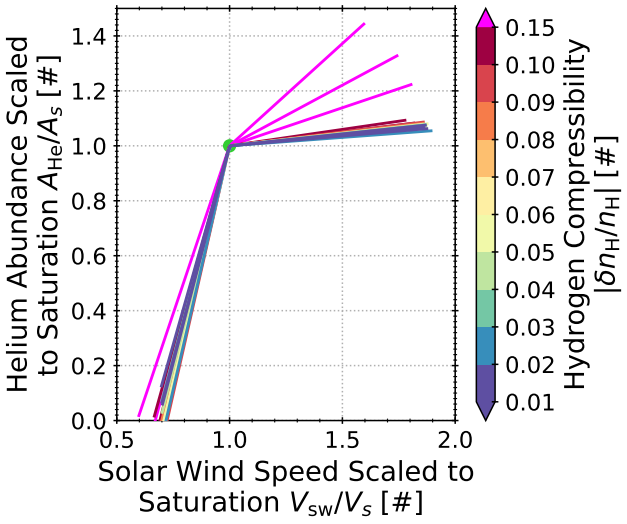

Figure 10. Fits to $A_{He}(v_{sw})$ in 15 $|\delta n_H/n_H|$ quantiles. Each fit is scaled to its situation point (v_s, A_s), which is indicated at $(1, 1)$ in green. As in Figure 9, the quantiles are indicated by the color bar.

The incompressible subset is approximately a line for which A_s decreases with increasing v_s, while the compressible subset does. To characterize the dependence of the saturation points on $|\delta n_H/n_H|$ without the parametric dependence in Figure 9, Figure 11 plots (a) the saturation speed v_s and (b) the saturation abundance A_s as a function of $|\delta n_H/n_H|$. The color scale matches Figures 9 and 10 and will be used going forward in all figures for which it is appropriate to facilitate comparison between plots. Additionally, markers for the two $|\delta n_H/n_H|$ subsets differ: incompressible quantiles are plotted with circles and compressible quantiles are plotted with squares. Markers corresponding to $|\delta n_H/n_H| = 0.085$ (see Figure 17) are indicated by their blue instead of black edge. The blue horizontal bands indicate points corresponding to the identified ranges of $|\sigma_c|$ in Figure 6 of Paper 1, the analogous analysis performed as a function of $|\sigma_c|$. From this figure we make the following observations about the saturation speed v_s.

1. The saturation speed is approximately constant for incompressible quantiles with $|\delta n_H/n_H| \leq 0.1$. The weighted average of values in this range are

$v_s = 428 \pm 1.4$ km s^{-1}, which corresponds to the *Low* $|\sigma_c|$ subset defined in Paper 1.

2. v_s increases slightly across the two largest incompressible $|\delta n_H/n_H|$ quantiles between $|\delta n_H/n_H| = 0.1$ and $|\delta n_H/n_H| = 0.15$.
3. For compressible quantiles with $|\delta n_H/n_H| > 0.15$, the maximum saturation speed increases to $v_s = 502 \pm 7$ km s^{-1} and average saturation speed increases markedly to $v_s = 461 \pm 3.4$ km s^{-1}.
4. The saturation speed belonging to the incompressible subset with the largest $|\delta n_H/n_H|$ is larger than the smallest v_s in the compressible subset.

For the saturation abundance A_s, we make the following observations.

1. The weighted average of A_s in the incompressible subset is $4.2 \pm 0.02\%$.
2. In the compressible subset, A_s
   (a) reaches a local minimum of $A_s = 3.9 \pm 0.1\%$ at $|\delta n_H/n_H| = 0.252$ and
   (b) a maximum value of $A_s = 4.13 \pm 0.1\%$ at $|\delta n_H/n_H| = 0.649$.
3. Incompressible A_s is larger than, or including error bars, within the range of A_s corresponding to *High* $|\sigma_c|$ in Paper 1.
4. Compressible A_s corresponding to the largest $|\delta n_H/n_H|$ falls within the range of A_s for *High* $|\sigma_c|$ in Paper 1, while compressible A_s corresponding to the other two $|\delta n_H/n_H| > 0.15$ quantiles fall within the A_s range corresponding to *Low* $|\sigma_c|$ in Paper 1.

To determine why non-Alfvénic A_{He} is greater than Alfvénic A_{He} for speeds $v_{sw} \gtrsim 545$ km s^{-1}, Figure 12 plots the gradients $\nabla_{v_{sw}} A_{He}$ for $v_{sw} > v_s$ (i.e. above the saturation point) as a function of $|\delta n_H/n_H|$. The style matches Figure 11. The marker indicating the slope at $|\delta n_H/n_H| = 0.085$ is marked with a light blue circle for comparison with Figure 17. This "saturation slope" (m_s) is approximately constant and independent of $|\delta n_H/n_H|$ in the incompressible subset with an average value 0.84 ± 0.06 10^{-3}% km^{-1} s. For the compressible subset, the saturation slope increases markedly and monotonically to a maximum of 2.7 ± 0.2 10^{-3}% km^{-1} s at $|\delta n_H/n_H| = 0.649$. This analysis suggests that $|\delta n_H/n_H| = 0.15$ may separate compressible and incompressible fluctuations in the solar wind, incompressible solar wind may have consistent behavior above saturation, and compressible fluctuations may introduce the apparent paradox in Figure 6.

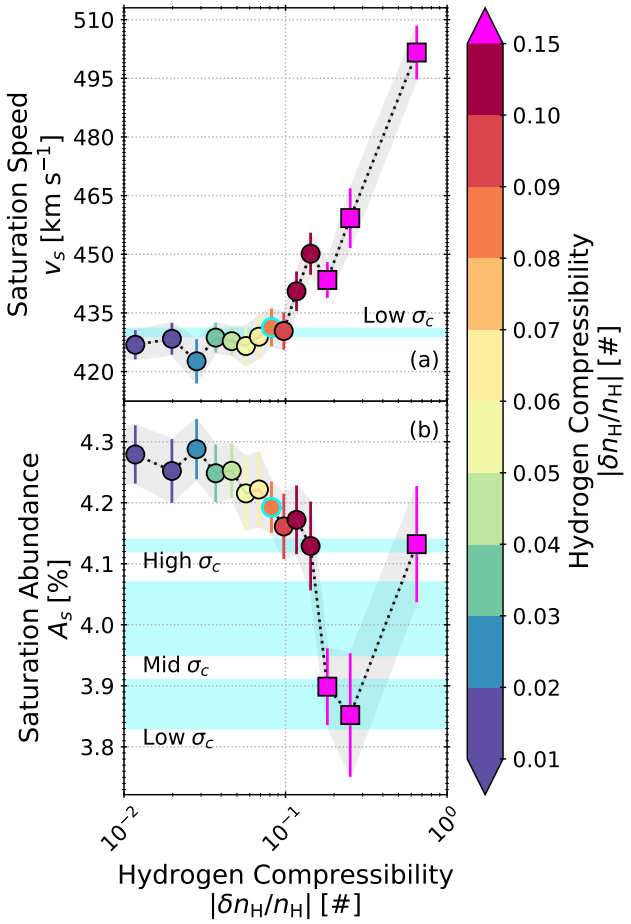

Figure 11. The saturation point (v_s, A_s) as a function of $|\delta n_H/n_H|$. Points are connected by a dotted line to aid the eye. Uncertainties are plotted as error bars with the same color as the markers and a semi-transparent gray envelope traces out the envelope surrounding the error bars. Markers are colored by $|\delta n_H/n_H|$ to facilitate comparison with other figures. As above, quantiles with $|\delta n_H/n_H| > 0.15$ are pink and square. The edge of the marker corresponding to the quantile for which $|\delta n_H/n_H| = 0.085$ is blue. The blue horizontal regions correspond to average value of (a) v_s and (b) A_{He} for key ranges of $|\sigma_c|$ derived in Paper 1.

3.4. *Excluding Compressive Solar Wind from* $A_{He}(v_{sw}, |\sigma_c|)$

To verify the significance of compressive solar wind in the saturation analysis of Paper 1, we repeat that analysis selecting incompressible solar wind with $|\delta n_H/n_H| <$ 0.15, 0.1, and 0.085. The first two are chosen based on Section 3.2. The latter is the contour of $|\delta n_H/n_H|$ in Figure 8 across which A_{He} in low $|\sigma_c|$ quantiles becomes larger than A_{He} in high $|\sigma_c|$ quantiles. We also select compressive solar wind with $|\delta n_H/n_H| > 0.15$. Figure 13 plots the resulting saturation (a) slopes, (b) speed, and

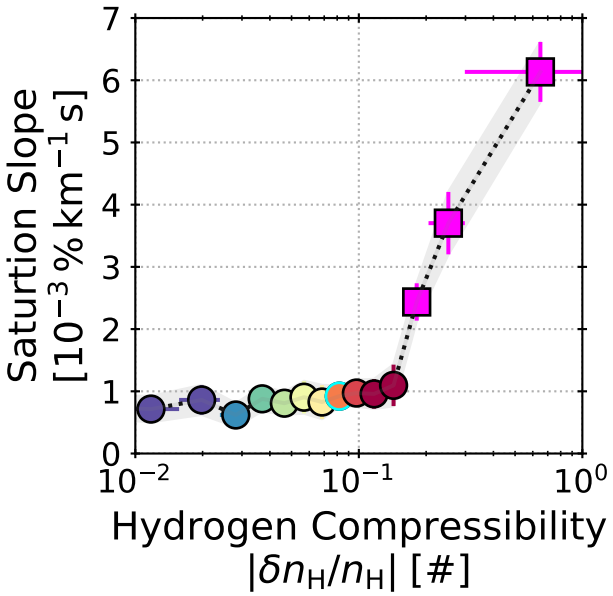

Figure 12. The slopes of $A_{\rm He}\,(v_{\rm sw})$ for speeds $v_{\rm sw} > v_s$ in each $|\delta n_{\rm H}/n_{\rm H}|$ quantile. Nominally, this is the slope for the fast solar wind nominally originating in open solar wind regions and we refer to them as "saturation slopes" in this work. Quantiles for which $|\delta n_{\rm H}/n_{\rm H}| > 0.15$ are plotted in pink and indicated with squares instead of circles. The marker indicating the quantile with $|\delta n_{\rm H}/n_{\rm H}| = 0.085$ is blue, while all other quantiles have a black marker edge.

(c) abundances. The incompressible observations with $|\delta n_{\rm H}/n_{\rm H}| < 0.085$, 0.1, and 0.15 are presented in dash-dotted red, green, and orange lines, respectively. The number of dots in the line increases with the threshold from 1 to 3. The compressible subset with $|\delta n_{\rm H}/n_{\rm H}| > 0.15$ is plotted with a dotted purple line. The fit parameters from all the data irrespective of threshold is plotted in a solid blue line. Shaded regions corresponding to the uncertainties for $|\delta n_{\rm H}/n_{\rm H}| < 0.1$, which is representative of all three incompressible subsets, and all $|\delta n_{\rm H}/n_{\rm H}|$ are shown. For visual clarity, the lines and uncertainties are smoothed with a Savitzky-Golay filter (Savitzky & Golay 1964; Steinier et al. 1972). The fit parameters themselves are given in Table 3. The solid gray lines are the fit parameters derived from Figure 1 across all observations.

In panel (a), we observe that all saturation slopes decrease with increasing $|\sigma_c|$. Comparing the compressible subset to all the data or any of the incompressible subsets show that the slopes in the compressible subset are a factor of 2 to 5x larger across $|\sigma_c|$. Comparison of the lines for any of the incompressible subsets along with all the data also shows that selecting data below any of the $|\delta n_{\rm H}/n_{\rm H}|$ thresholds reduce m_s and this change is

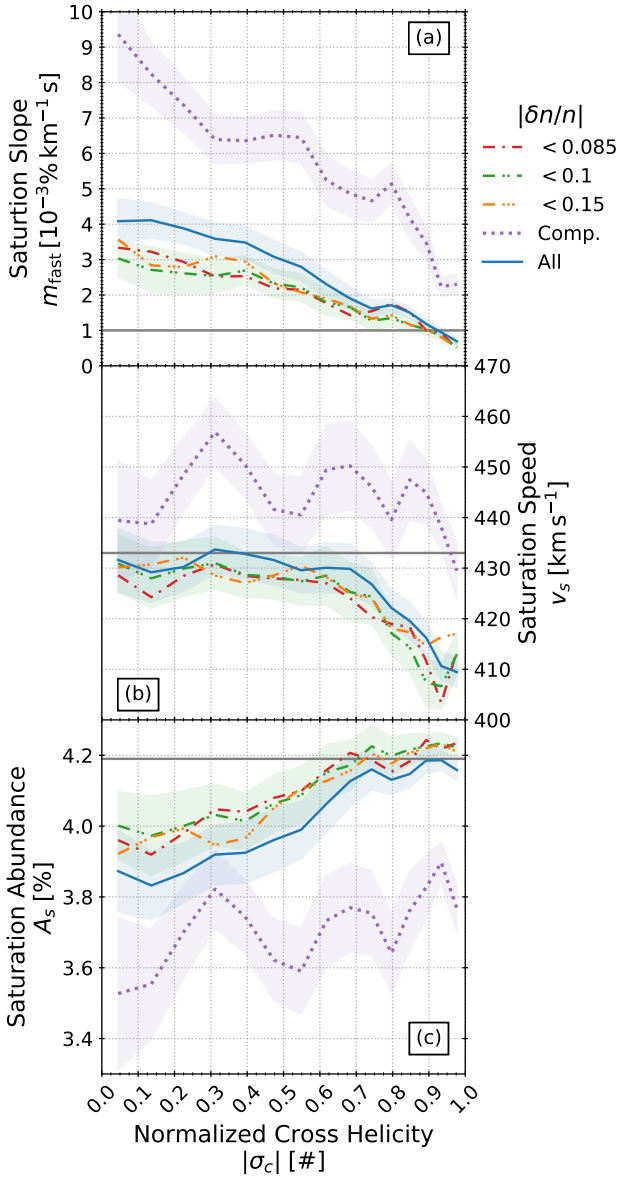

Figure 13. Saturation fit parameters for different maximum $|\delta n_{\rm H}/n_{\rm H}|$, given by the legend, as a function of $|\sigma_c|$ along with the data, irrespective of $|\delta n_{\rm H}/n_{\rm H}|$, from Paper 1. The panels are saturation **(a)** slope (m_s), **(b)** speed (v_s), and **(c)** abundance (A_s). Gray lines are the fit parameters across all observations in Figure 1. The *Comp.* subset is compressible solar wind with $|\delta n_{\rm H}/n_{\rm H}| > 0.15$.

most significant for $|\sigma_c| < 0.4$. Comparing these trends to the gray line, we also observe that m_s in Figure 1 is closest to Alfvénic m_s incompressible solar wind or all the observations, irrespective of compressibility.

In panels (b), compressible v_s is less than 10% larger than any of the incompressible subsets of all the data. However, it also typically exceeds v_s derived in Figure 1 (gray line). In contrast, v_s for the incompressible subsets

	Saturation Slope m_s $[10^{-3}\%\,\mathrm{km^{-1}\,s}]$				Vanishing Speed v_0 $[\mathrm{km\,s^{-1}}]$			
$\lvert\sigma_c\rvert$	0.085	0.1	0.15	Comp.	0.085	0.1	0.15	Comp.
0.05	3.4 ± 0.5	3.4 ± 0.7	3.6 ± 0.6	8.3 ± 1.6	301 ± 4	301 ± 4	301 ± 4	320 ± 8
0.14	3.5 ± 0.5	2.9 ± 0.6	2.8 ± 0.6	8.4 ± 0.8	302 ± 4	302 ± 4	302 ± 4	316 ± 4
0.22	2.8 ± 0.6	2.7 ± 0.6	2.9 ± 0.6	7.7 ± 0.9	298 ± 5	298 ± 4	300 ± 4	313 ± 4
0.31	2.8 ± 0.4	2.7 ± 0.4	3.1 ± 0.4	7.0 ± 0.6	291 ± 5	293 ± 4	296 ± 4	306 ± 4
0.39	2.2 ± 0.4	2.4 ± 0.4	3.0 ± 0.5	5.7 ± 0.6	302 ± 7	297 ± 4	300 ± 7	306 ± 4
0.47	2.5 ± 0.4	2.7 ± 0.3	2.2 ± 0.5	6.5 ± 0.8	293 ± 5	296 ± 4	299 ± 5	319 ± 5
0.55	2.0 ± 0.4	1.8 ± 0.4	1.9 ± 0.4	6.7 ± 0.8	298 ± 11	296 ± 5	298 ± 4	309 ± 5
0.62	2.1 ± 0.4	2.3 ± 0.4	2.3 ± 0.4	5.3 ± 0.6	293 ± 5	293 ± 5	295 ± 6	308 ± 8
0.68	1.4 ± 0.3	1.3 ± 0.3	1.3 ± 0.3	5.2 ± 0.7	295 ± 13	285 ± 13	299 ± 5	304 ± 10
0.74	1.3 ± 0.3	1.5 ± 0.3	1.7 ± 0.2	5.4 ± 0.5	294 ± 5	295 ± 4	297 ± 4	309 ± 7
0.8	2.3 ± 0.5	1.3 ± 0.2	1.3 ± 0.2	4.3 ± 0.5	279 ± 23	280 ± 13	277 ± 11	308 ± 10
0.85	1.2 ± 0.2	1.2 ± 0.2	1.3 ± 0.2	5.1 ± 0.7	266 ± 14	296 ± 4	298 ± 4	287 ± 8
0.89	1.0 ± 0.1	0.9 ± 0.2	0.9 ± 0.1	2.6 ± 0.3	279 ± 12	282 ± 16	268 ± 14	299 ± 9
0.93	1.0 ± 0.1	0.9 ± 0.1	0.9 ± 0.1	3.3 ± 0.3	291 ± 11	293 ± 10	275 ± 15	305 ± 5
0.98	0.5 ± 0.1	0.5 ± 0.1	0.6 ± 0.1	2.6 ± 0.2	253 ± 16	253 ± 16	260 ± 14	284 ± 7
Avg	1.2 ± 0.1	1.2 ± 0.1	1.1 ± 0.1	4.0 ± 0.1	420.0 ± 2.0	421.0 ± 1.0	424.0 ± 1.0	443.0 ± 1.0

	Saturation Speed v_s $[\mathrm{km\,s^{-1}}]$				Saturation Abundance A_s [%]			
$\lvert\sigma_c\rvert$	0.085	0.1	0.15	Comp.	0.085	0.1	0.15	Comp.
0.05	428 ± 5	429 ± 6	430 ± 6	441 ± 13	3.94 ± 0.08	3.95 ± 0.1	3.9 ± 0.1	3.59 ± 0.23
0.14	423 ± 5	428 ± 6	431 ± 6	436 ± 7	3.88 ± 0.09	3.95 ± 0.11	3.97 ± 0.11	3.5 ± 0.14
0.22	429 ± 6	430 ± 6	431 ± 6	444 ± 8	3.99 ± 0.1	3.98 ± 0.1	3.95 ± 0.1	3.59 ± 0.14
0.31	432 ± 5	432 ± 5	431 ± 5	456 ± 6	4.03 ± 0.08	4.02 ± 0.08	3.97 ± 0.08	3.74 ± 0.1
0.39	428 ± 6	429 ± 5	428 ± 6	458 ± 6	4.06 ± 0.08	4.03 ± 0.08	3.94 ± 0.09	3.8 ± 0.1
0.47	427 ± 5	427 ± 4	431 ± 5	439 ± 7	4.02 ± 0.09	3.99 ± 0.07	4.08 ± 0.11	3.56 ± 0.13
0.55	427 ± 6	430 ± 4	431 ± 4	441 ± 8	4.1 ± 0.08	4.14 ± 0.08	4.11 ± 0.08	3.53 ± 0.12
0.62	425 ± 5	425 ± 5	427 ± 6	450 ± 8	4.09 ± 0.08	4.07 ± 0.08	4.05 ± 0.09	3.68 ± 0.11
0.68	426 ± 6	429 ± 7	427 ± 5	450 ± 9	4.2 ± 0.08	4.21 ± 0.07	4.19 ± 0.07	3.7 ± 0.12
0.74	420 ± 5	420 ± 4	421 ± 4	444 ± 7	4.21 ± 0.07	4.18 ± 0.06	4.14 ± 0.06	3.62 ± 0.1
0.8	417 ± 8	422 ± 5	428 ± 4	444 ± 8	4.06 ± 0.1	4.19 ± 0.05	4.2 ± 0.05	3.69 ± 0.11
0.85	421 ± 5	410 ± 4	411 ± 4	439 ± 9	4.21 ± 0.04	4.18 ± 0.04	4.16 ± 0.05	3.55 ± 0.13
0.89	412 ± 4	413 ± 6	421 ± 5	452 ± 7	4.23 ± 0.03	4.23 ± 0.04	4.23 ± 0.03	3.89 ± 0.08
0.93	403 ± 4	403 ± 4	412 ± 6	428 ± 4	4.2 ± 0.03	4.2 ± 0.03	4.19 ± 0.03	3.66 ± 0.06
0.98	414 ± 4	414 ± 4	414 ± 4	433 ± 6	4.22 ± 0.03	4.21 ± 0.03	4.18 ± 0.03	3.65 ± 0.05
Avg	420.0 ± 1.0	421.0 ± 1.0	424.0 ± 1.0	443.0 ± 2.0	4.17 ± 0.01	4.17 ± 0.01	4.16 ± 0.01	3.68 ± 0.03

Table 3. Saturation fit parameters for incompressible observations with $|\delta n_\mathrm{H}/n_\mathrm{H}| < 0.085$, 0.1, 0.15 along with compressible $|\delta n_\mathrm{H}/n_\mathrm{H}| > 0.15$, under *Comp.* columns. The bottom row is the weighted average for each column.

along with all the data are nearly indistinguishable and well below v_s indicated by the gray line for $|\sigma_c| > 0.75$.

Panel (c) shows that compressible A_s is at most 16% smaller than all other saturation abundances. The mean values of A_s for the incompressible subsets (green, red, and orange lines) are larger than the mean value of A_s across all data (blue line), their mutual uncertainties overlap. For non-Alfvénic solar wind with $|\sigma_c| < 0.6$, all incompressible subsets along with all the data irrespective of compressibility have $A_s < 4.19\%$, which is below A_s in Figure 1 (gray line), but A_s in incompressible Alfvénic solar wind with $|\sigma_c| \geq 0.683$ is (excluding $|\sigma_c| = 0.74$ for $|\delta n_{\rm H}/n_{\rm H}| < 0.85$) within 1% of $A_s = 4.19\%$ from Figure 1. That A_s in compressible solar wind is larger than A_s in incompressible solar wind suggests that the increase in m_s with decreasing $|\delta n_{\rm H}/n_{\rm H}|$ in Figures 9 and 10 drives A_s to smaller values and v_s to larger values. This suggests that there is a subset of solar wind with an enhanced $A_{\rm He}$ that is related to compressive fluctuations and that obscures the transition in our observations from slow to fast wind. This analysis also confirms that $|\delta n_{\rm H}/n_{\rm H}| = 0.15$ is a threshold across which the solar wind transitions from compressible to incompressible.

3.5. *Visualizing the Speed Ranges on the Bimodal Distribution of $v_{\rm sw}$ Observed During Solar Minima*

The classification of solar wind into slow and fast subsets is based, in part, on the bimodal nature of the distribution of speeds observed at 1 AU during solar minima. Although this classification is known to be limited in both precision and accuracy, it relies solely on observations of $v_{\rm sw}$, which most spacecraft provide. Alterman (2025) quantify the location and width of these peaks by fitting the slow wind distribution with $v_{\rm sw} < 400$ km s^{-1} and the fast wind distribution with $v_{\rm sw} > 600$ km s^{-1} each to a Gaussian. The speeds are $v_{\rm slow} = 355 \pm 44$ km s^{-1} and $v_{\rm fast} = 622 \pm 59$ km s^{-1}. Alterman (2025) show that the range of near-Earth $v_{\rm sw}$ predicted from near-Sun observations of the solar wind's kinetic energy flux (Liu et al. 2021) is $v_K = 557$ to 700 km s^{-1}. The same work shows that the range of speeds to which solar wind from continuously open source regions would be accelerated in the absence of Alfvén wave forcing in transit, i.e. "wave-poor" fast wind in which the energy in the Alfvénic fluctuations is less than typical fast wind, is $v_{IP} = 435$ to 554 km s^{-1}. Figure 1 of Alterman (2025) contextualizes these observations by highlighting the relevant segments of the $v_{\rm sw}$ probability distribution function (PDF) for observations collected during solar minima. Paper 1 determines

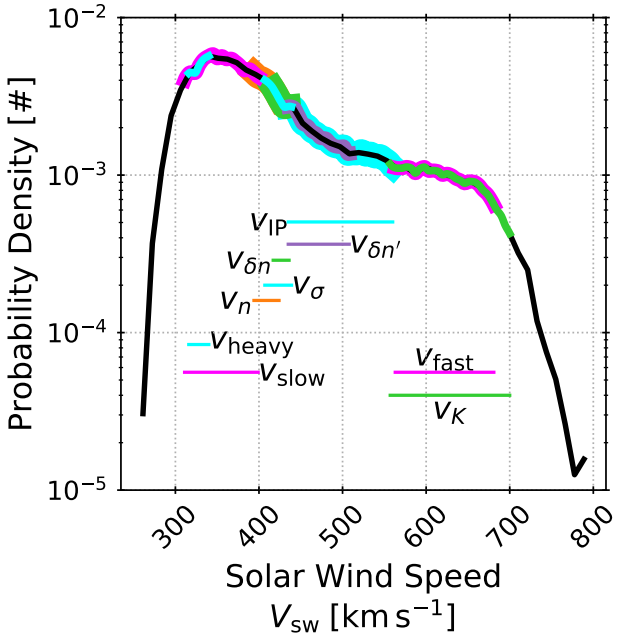

Figure 14. The probability density function (PDF) of the solar wind speed observed by the Wind Faraday cups at 1 AU during solar minima 23 and 24 is plotted in black. The colored segments indicate speed ranges derived in this paper, Paper 1, Alterman et al. (2024), and Alterman (2025). The $v_{\rm sw}$ range corresponding to each segment is plotted in the same color below the PDF and labeled. The vertical location of these $v_{\rm sw}$ ranges is chosen to avoid overlap. The speed ranges are summarized in Table 4.

that $v_\sigma = 407$ to 439 km s^{-1} is the range of speeds over which the solar wind transitions from its slow to fast state when characterized by $\nabla_{v_{\rm sw}} A_{\rm He}$ across 15 $|\sigma_c|$ quantiles. Paper 1 also shows that $n_{\rm He}(v_{\rm sw})$ peaks at speeds $v_n = 409 \pm 15$ km s^{-1}. Figure 8 of Paper 1 contextualizes v_σ and v_n in the same way as Alterman (2025) using the PDF of $v_{\rm sw}$ observations collected during solar minima. The range of speeds over which heavy ion abundances saturate is $v_{\rm heavy} = 316$ to 340 km s^{-1} (Alterman et al. 2024).

Figure 14 synthesizes three versions of this histogram with the above speeds (Alterman 2025; Paper 1; Alterman et al. 2024) and adds the range of speeds at which the slow/fast wind transition occurs across the 15 $|\delta n_{\rm H}/n_{\rm H}|$ quantiles derived in this paper. Table 4 summarizes these speeds. The PDF is plotted in black. Each speed range is highlighted with a color with line thickness chosen so that overlapping segments are all visible. Because this figure identifies nine overlapping speed intervals, each segment is also plotted below the PDF and labeled here. The vertical location of these labeled segments is chosen so that the labels do not overlap, but are not significant otherwise. The tran-

Table 4. Key speeds highlighted in Figure 14.

Speed	Typical Value $[\mathrm{km\,s^{-1}}]$	Description
v_K	557 to 700	The range of speeds predicted near-Earth from the radial gradient of the solar wind's kinetic energy flux[a] observed with Parker Solar Probe near-Sun observations[b].
v_{fast}	622 ± 59	The fast wind peaks during solar minima[c].
v_{IP}	434 to 554	The range of speeds predicted for fast wind observed at 1 AU if Alfvén wave forcing had been absent during solar wind propagation, i.e. "wave-poor" solar wind from continuously open source regions in which the energy in the Alfvénic fluctuations is less than typical fast wind.[d].
$v_{\delta n'}$	435 to 508	The range of compressible saturation speeds.
$v_{\delta n}$	417 to 436	The range of incompressible saturation speeds.
v_σ	407 to 439	The range of saturation speeds across 15 quantiles in $\lvert\sigma_c\rvert$[e].
v_n	409 ± 15	The range of speeds corresponding to the peak of n_{He} as a function of v_{sw}[f].
v_{slow}	355 ± 44	The slow wind peak during solar minima[g].
v_{heavy}	316 to 340	The range of heavy element abundance saturation speeds[h].

[a] Alterman (2025)
[b] Liu et al. (2021)
[c] Paper 1
[d] Paper 1
[e] Paper 1
[f] Paper 1
[g] Paper 1
[h] Alterman et al. (2024)

sition between slow and fast wind for incompressible solar wind ($|\delta n_{\mathrm{H}}/n_{\mathrm{H}}| < 0.15$) is labeled $v_{\delta n} = 417$ to $436\ \mathrm{km\,s^{-1}}$. The transition for compressible solar wind ($|\delta n_{\mathrm{H}}/n_{\mathrm{H}}| > 0.15$) is labeled $v_{\delta n'} = 435$ to $508\ \mathrm{km\,s^{-1}}$.

Figure 14 shows that the speeds are organized in the following increasing order.

1. The slow wind peak v_{slow} covers the lowest range of speeds.
2. The range of speeds at which the gradients of heavy ion abundances transition from slow to fast wind (v_{heavy}) is within the slower portion of the range v_{slow}, but does not exceed the center of the slow wind peak (Alterman et al. 2024).
3. The range of speeds v_n at which the helium number density peaks as a function of v_{sw} derived in Paper 1 overlaps with the fast end of v_{slow}.
4. The saturation speed v_σ derived across $|\sigma_c|$ quantiles overlaps with v_n, but the slowest v_σ is faster than the fastest v_{slow}.
5. The incompressible saturation speed $v_{\delta n}$ overlaps with both the fast end of the v_n range and the majority of the v_σ range.
6. The range of compressible saturation speeds $v_{\delta n'}$ overlaps with v_n by $4\ \mathrm{km\,s^{-1}}$. By construction, the slowest $v_{\delta n'}$ is faster than the fastest $v_{\delta n}$.
7. The range of speeds v_{IP} corresponding to Alfvén "wave-poor" fast wind, which is likely synonymous with Alfvénic slow wind, effectively spans the range of speeds from $v_{\delta n}$ to the lower range of v_{fast} and v_K.
8. The range of near-Earth speeds derived from the near-Sun radial gradients of the solar wind's total and kinetic energy fluxes (v_K) corresponds to and exceeds the fast wind peak (v_{fast}).

Although not plotted, the range of speeds in Figure 6 over which non-Alfvénic A_{He} ($|\sigma_c| < 0.7$) exceed Alfvénic A_{He} ($|\sigma_c| > 0.7$) is $530 - 560\ \mathrm{km\,s^{-1}}$, which corresponds to the gap between $v_{\delta n'}$ and the lower bounds of v_K and v_{fast}. This analysis suggests that compressive fluctuations are significant in the $v_{\delta n'}$ region of the v_{sw} PDF, where the power in Alfvénic fluctuations is reduced in comparison to typical fast wind (Alterman 2025) (which may be related to the Alfvénic slow wind), and which corresponds to the intermediate range of speeds over which the literature specifies ad hoc speeds for transitioning from slow to fast wind, with the implied change in solar source region.

3.6. *Contextualizing Observed v_{sw} and A_{He} in the $(|\sigma_c|, |\delta n_{\mathrm{H}}/n_{\mathrm{H}}|)$ Plane*

Alfvénic and compressive fluctuations are mutually exclusive. As such, solar wind is broadly considered to be incompressible and incompressible solar wind is broadly considered to be Alfvénic, but these relationships do not imply that incompressible and Alfvénic solar wind are interchangeable nor that compressible and non-Alfvénic solar wind are interchangeable without carefully considering data selection and solar wind conditions. Figure 15 presents contour plots of (a) mean, (b) 90% quantile, and (c) 10% quantile of $A_{\mathrm{He}}\,(|\sigma_c|, |\delta n_{\mathrm{H}}/n_{\mathrm{H}}|)$ along with (d) the variability of A_{He}. This variability is referenced to the mean value

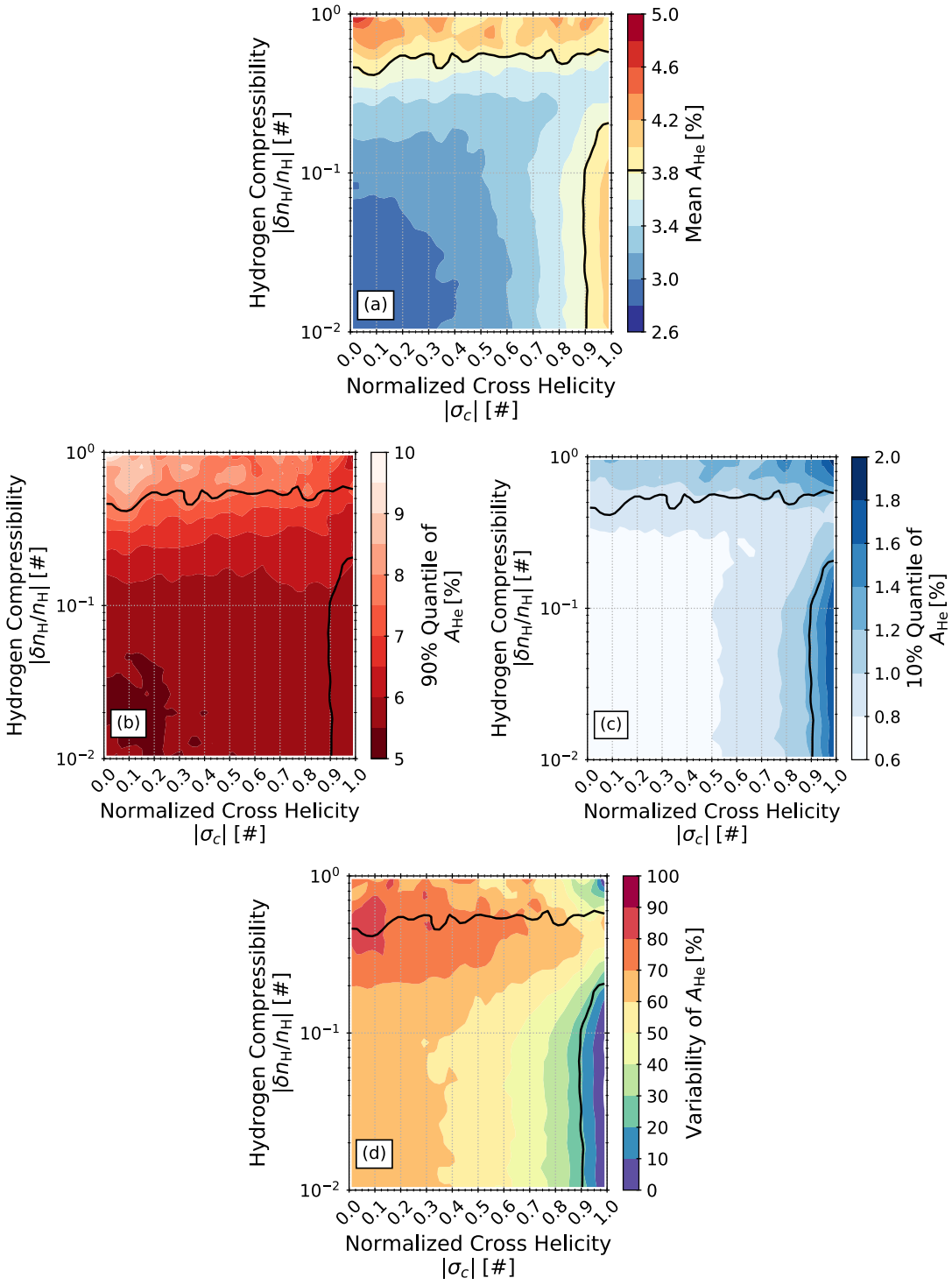

Figure 15. Contour plots of the **(a)** mean, **(b)** 90% quantile, and **(c)** 10% quantile of the helium abundances as a function of cross helicity and solar wind compressibility. Panel **(d)** plots the variability of the helium abundance. The black contours in all panels indicate $A_{He} = 3.82\%$ from panel (a), which is the smallest A_s derived in Paper 1 and this work. All contours are smoothed with a 1σ Guassian kernel for visual clarity. While the ranges for the color scales in panels (a) to (c) are different, the color scales themselves are chosen to provide visual continuity such that the 90% quantiles in panel (b) are plotted in red to match colors at the high A_{He} range of panel (a) and the 10% quantiles in panel (c) are plotted in blue to match the low A_{He} range in panel (a).

and calculated as

$$100 \times \left(\frac{90\%\,\text{quantile} - 10\%\,\text{quantile}}{\text{mean}} - 1 \right). \quad (6)$$

A variability > 1 indicates that the distance between the 90% and 10% quantiles is larger than the mean value. A variability < 1 indicates that the distance between the quantiles is less than the mean value. Visually, this is how much the difference between panels (b) and (c) exceeds the values in panel (a), normalized to that panel. All contours are smoothed by a 1σ Gaussian kernel for visual clarity. The black contours are $A_{\rm He} = 3.82\%$ derived in panel (a), where 3.82% is the smallest A_s in both this work and Paper 1.

In panel (a), we observe two distinct populations of $A_{\rm He} \geq A_s$. A low compressibility subset with high cross helicity occupies the right side of the figure. We will refer to this as the helium-rich, Alfvénic subset. A high compressibility subset without a preferred cross helicity occupies the top of the figure. We refer this as the helium-rich, compressive subset. There is also a helium-poor subset with $A_{\rm He} < A_s\%$ that occupies the majority of the plane outside of these two helium-rich regions. Comparing panels (b) and (c), we observe that the 90% quantile of this high compressibility subset exceeds $A_{\rm He} = 7.5\%$, while the 10% quantile only exceeds $A_{\rm He} = 1.4\%$ in Alfvénic wind with $|\sigma_c| \gtrsim 0.7$. In contrast, the 90% quantile of the low compressibility subset has, effectively, $A_{\rm He} < 6\%$ and the 10% quantile exceeds $A_{\rm He} = 1.4\%$ across the range of $|\delta n_{\rm H}/n_{\rm H}|$ in this subset. The variability in panel (d) quantifies this comparison of the 90% and 10% quantiles. It shows that in this incompressible subset, $A_{\rm He}$, for which the average is above saturation ($A_{\rm He} > A_s$), the variability is within approximately 20% of the mean value. In contrast, the variability in the compressible subset exceeds 70%.

Figure 16 is an abridged presentation of the analogous analysis of $v_{\rm sw}$. Panel (a) plots mean $v_{\rm sw}$ and Panel (b) plots the variability of $v_{\rm sw}$ calculated in the same manner as Figure 15. Both panels include contours of mean $v_{\rm sw} = 433$ and 450 km s^{-1}. $v_s = 450$ km s^{-1} is the largest v_s in this work for $|\delta n_{\rm H}/n_{\rm H}| < 0.15$. $v_s = 433$ km s^{-1} is the least Alfvénic and fastest v_s in Paper 1 and within a few km s^{-1} of incompressible v_s calculated in this work. Comparing panel (a) in Figures 15 and 16, we see that $v_{\rm sw} > v_s$ corresponds to the incompressible, Alfvénic, and helium-rich subset of $A_{\rm He}$ in Figure 15. Panel (a) also shows that mean $v_{\rm sw}$ only exceeds the largest (incompressible) v_s in the incompressible subset. Panel (b) shows that mean $v_{\rm sw}$ in the Alfvénic subset is more variable than in the compressible subset. Comparing panels (b) and (d) in Figure 15 to panel (b) in Figure 16, we observe that that the largest

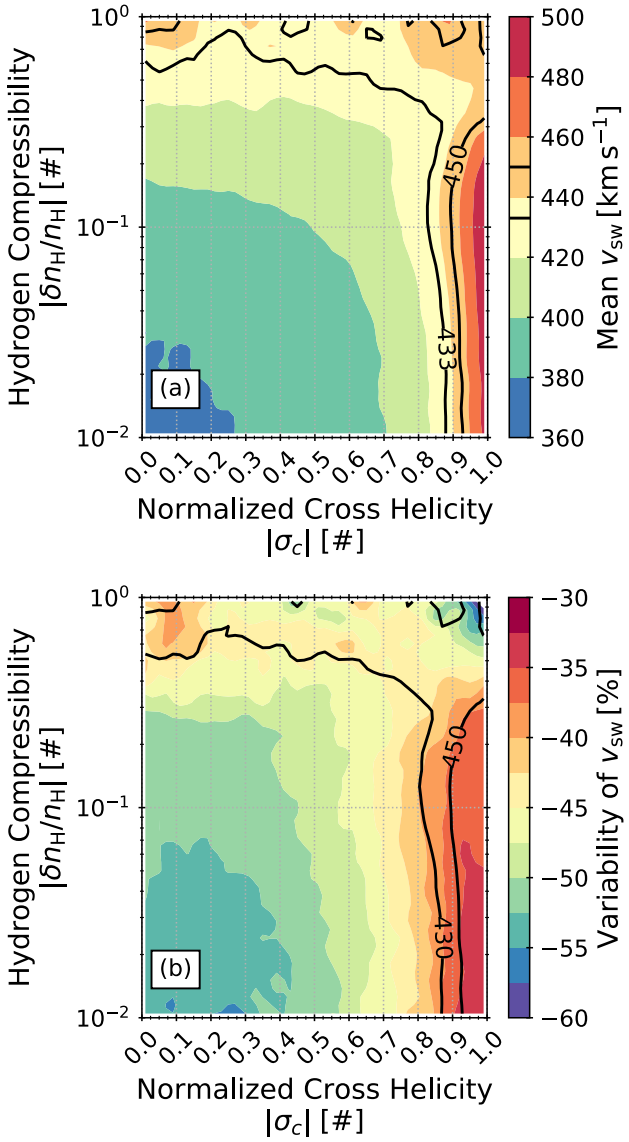

Figure 16. (a) The solar wind speed as a function of cross helicity and compressibility. The black contour indicates $v_{\rm sw} = 433$ and 450 km s^{-1}, the fastest v_s derived in Paper 1 and the fastest v_s derived for incompressible solar wind ($|\delta n_{\rm H}/n_{\rm H}| < 0.15$) in this work. **(b)** The variability of $v_{\rm sw}$ calculated in the same manner as in Figure 15.

$A_{\rm He}$ coincide with the most variable $A_{\rm He}$ in the compressible subset where the variability in mean $v_{\rm sw}$ is not as large as in the Alfvénic subset. This implies that the compressibility is driving the changes in $A_{\rm He}$, not $v_{\rm sw}$ itself. Comparing panel (a) and (b) here, we also observe the expected anti-correlation between $|\sigma_c|$ and $|\delta n_{\rm H}/n_{\rm H}|$ along contours of constant average $v_{\rm sw}$, even though $v_{\rm sw}$ may be highly variable at any given point across most of the plane. This suggests that a wide range of $v_{\rm sw}$ can be observed in both incompressible, Alfvénic solar wind and

compressible, non-Alfvénic solar wind and these ranges of speeds are largely overlapping, which may explain the apparent paradox presented in Sections 3.1 and 3.2.

3.7. *Contextualizing Observed* $|\delta n_H/n_H|$ *in the* $(|\sigma_c|, A_{He})$ *Parameter Space*

Broadly, slow and fast solar wind are accelerated in different types of solar wind source regions. Fast wind emerges from solar wind source regions like CHs with magnetic fields that are continuously open to the heliosphere. Slow wind emerges from solar wind source regions that are only intermittently open to the heliosphere, e.g. pseudostreamers, helmet streamers, etc. These latter regions are sometimes colloquially referred to as magnetically "closed". As reviewed in Section 1, a variety of observations show that this classification scheme is overly general. Per Paper 1 and as illustrated in Figure 3, classifying *in situ* solar wind observations as in the $(|\sigma_c|, A_{He})$-plane space may separate solar wind by the magnetic topology source region of the solar source region from which it observes. Generally, helium-poor solar wind without a preferred $|\sigma_c|$ corresponds to solar wind from magnetically closed regions. In contrast, helium-rich and Alfvénic solar wind originates in magnetically open source regions.

Solar wind from magnetically closed regions is often slower than solar wind from magnetically open regions. However, this is not always the case. The Alfvénic slow wind (ASW) is an emerging class of solar wind that is most similar to fast wind in all respects except its speed, which is more typical of slow wind (D'Amicis et al. 2021b,a; D'Amicis et al. 2018, 2016; D'Amicis & Bruno 2015; Yardley et al. 2024; Rivera et al. 2025). Alterman (2025) suggests that ASW may be wave-poor solar wind from continuously open source regions in which the energy in the Alfvénic fluctuations is reduced in comparison to typical fast wind.. Consistent with these works, Paper 1 argues that ASW is the slow speed extension of solar wind originating in magnetically open sources and this range of speeds is slower than the maximum speed that solar wind from magnetically closed source can obtain. To compare our observations of $|\delta n_H/n_H|$ with the results of Paper 1, we now contextualize the compressibility in the $(|\sigma_c|, A_{He})$ parameter space.

Figure 17 plots (a) mean and (b) the 75% quantile of $|\delta n_H/n_H|$ as a function of $|\sigma_c|$ and A_{He}. Solid black contours in panel (a) indicate $|\delta n_H/n_H| = 0.085$, 0.1, and 0.15, the three thresholds for separating incompressible and compressible solar wind that we have identified in this work. The dash-dotted black line indicates where the 75% quantile of $|\delta n_H/n_H| = 0.15$ in panel (b). In panel (b), the solid contours indicate where

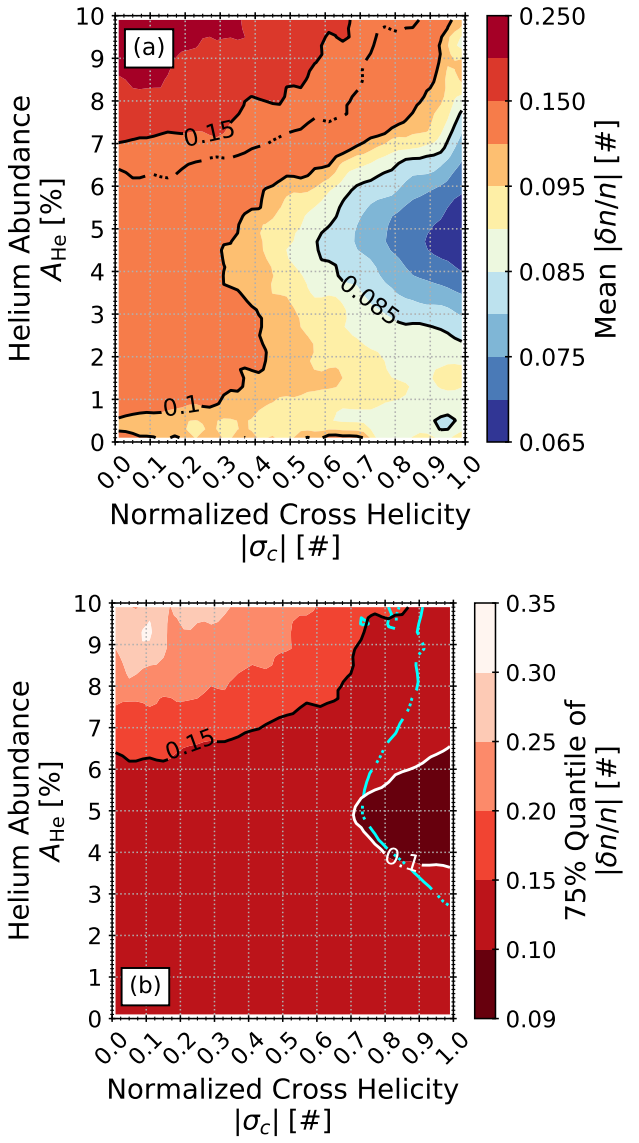

Figure 17. Contour plots of **(a)** mean and **(b)** 75% quantile $|\delta n_H/n_H|$ as a function of $|\sigma_c|$ and A_{He}. Contours are smoothed with a 1σ Gaussian kernel for visual clarity. Solid black contours in panel (a) indicate $|\delta n_H/n_H| = 0.085$, 0.1, and 0.15. The dash-dotted black contour indicates where the 75% quantile of $|\delta n_H/n_H| = 0.15$ in panel (b). Solid contours in panel (b) indicate where the 75% quantile of $|\delta n_H/n_H| = 0.1$ and 0.15. The region of the plane with $|\sigma_c|$ greater than that indicated by the dash-dotted blue line corresponds to solar wind originating in continuously open source regions as defined in Paper 1.

the 75% quantiles of $|\delta n_H/n_H| = 0.1$ and 0.15. Solar wind with $|\sigma_c|$ greater than that indicated by the dash-dotted blue line is in the region of the plane identified in Paper 1 as originating in magnetically open source regions. Here, we observe that solar wind car-

$\lvert\delta n_H/n_H\rvert$	$\lvert\sigma_c\rvert\,(A_s, \lvert\delta n_H/n_H\rvert)$ [#]	$\lvert\sigma_c\rvert\,(v_s, \lvert\delta n_H/n_H\rvert)$ [#]
0.003	0.660 ± 0.003	0.610 ± 0.003
0.012	0.661 ± 0.003	0.610 ± 0.003
0.020	0.661 ± 0.003	0.607 ± 0.003
0.028	0.661 ± 0.003	0.607 ± 0.003
0.037	0.663 ± 0.003	0.604 ± 0.003
0.046	0.663 ± 0.003	0.603 ± 0.003
0.057	0.661 ± 0.003	0.603 ± 0.003
0.068	0.660 ± 0.003	0.597 ± 0.003
0.082	0.652 ± 0.003	0.600 ± 0.003
0.098	0.649 ± 0.003	0.593 ± 0.003
0.117	0.642 ± 0.003	0.591 ± 0.003
0.143	0.624 ± 0.003	0.585 ± 0.004
0.182	0.600 ± 0.003	0.559 ± 0.003
0.252	0.558 ± 0.004	0.530 ± 0.004
0.649	0.490 ± 0.004	0.493 ± 0.005

Table 5. The mappings from $\lvert\delta n_H/n_H\rvert$ to $\lvert\sigma_c\rvert$. The first column is $\lvert\sigma_c\rvert$ corresponding to v_s in a given $\lvert\delta n_H/n_H\rvert$ quantile (Figures 19 and 22 (a)). The second columns is $\lvert\sigma_c\rvert$ corresponding to A_s in a given $\lvert\delta n_H/n_H\rvert$ quantile (Figures 18 and 22 (b)).

$\lvert\sigma_c\rvert$	$\lvert\delta n_H/n_H\rvert\,(A_s, \lvert\sigma_c\rvert)$ [#]	$\lvert\delta n_H/n_H\rvert\,(v_{sw}, \lvert\sigma_c\rvert)$ [#]
0.98	0.069 ± 0.001	0.08 ± 0.001
0.89	0.071 ± 0.001	0.08 ± 0.001
0.93	0.072 ± 0.001	0.082 ± 0.001
0.85	0.074 ± 0.001	0.084 ± 0.001
0.80	0.078 ± 0.001	0.085 ± 0.001
0.74	0.08 ± 0.001	0.089 ± 0.001
0.68	0.082 ± 0.001	0.093 ± 0.001
0.62	0.087 ± 0.002	0.097 ± 0.001
0.55	0.088 ± 0.001	0.104 ± 0.002
0.47	0.095 ± 0.002	0.106 ± 0.002
0.39	0.097 ± 0.002	0.114 ± 0.002
0.31	0.099 ± 0.002	0.122 ± 0.002
0.22	0.104 ± 0.002	0.13 ± 0.003
0.05	0.106 ± 0.002	0.135 ± 0.003
0.14	0.11 ± 0.003	0.132 ± 0.004

Table 6. Quantiles of $\lvert\sigma_c\rvert$ derived in Paper 1 mapped to $\lvert\delta n_H/n_H\rvert$ using Figures 20 and 21. Paper 1, Table 1 gives v_s, A_s, m_s, and v_0 derived in $\lvert\sigma_c\rvert$ quantiles.

rying compressive fluctuations largely occupies the top left corner of the plane where the minimum A_{He} along the $\lvert\delta n_H/n_H\rvert = 0.15$ contour is more than 7% (in panel a) and 6% (in panel b), both larger than $A_s = 4.34\%$, the largest A_s in this work and Paper 1 accounting for uncertainty on A_s. On the right side of panel (b), the 75% quantile of the solar wind compressibility in the central portion of the open field region (bounded on the left by the blue dash-dotted line, Paper 1) does not exceed $\lvert\delta n_H/n_H\rvert = 0.1$ and the majority of this plane does not exceed $\lvert\delta n_H/n_H\rvert = 0.15$, the largest threshold we identified for the separation between incompressible and compressible solar wind based only on $\nabla_{v_{sw}} A_{He}\,(v_{sw} > v_s)$. In panel (a), mean $\lvert\delta n_H/n_H\rvert$does not exceed 0.085 in a slightly larger region of the plane. Based on the source region identification in Paper 1, this analysis suggests that solar wind is from continuously open sources is incompressible and solar wind from intermittently open source regions has a compressibility that approaches the $\lvert\delta n_H/n_H\rvert = 0.15$ threshold. Forthcoming work shows that transients are located at a compressibility $\lvert\delta n_H/n_H\rvert > 0.15$ in panel (a) (Alterman & D'Amicis 2025b).

3.8. *Mapping Between $\lvert\delta n_H/n_H\rvert$ and $\lvert\sigma_c\rvert$*

We have shown an enhancement in helium abundance $A_{He} > A_s$ in two different, non-overlapping regions of the $(\lvert\sigma_c\rvert, \lvert\delta n_H/n_H\rvert)$-plane: one compressible and one Alfvénic. While the Alfvénic subset of enhanced A_{He} is limited to $\lvert\delta n_H/n_H\rvert < 0.2$, the compressible subset is observed across all $\lvert\sigma_c\rvert$. Despite the physical definition of Alfvénic fluctuations, compressible solar wind is not interchangeable with non-Alfvénic solar wind. Rather both processes must be considered because statistical aggregation across a range of solar wind conditions mixes these two types of plasma. This is why our analysis shows that the saturation fits across $\lvert\delta n_H/n_H\rvert$ or $\lvert\sigma_c\rvert$ quantiles averages over variability in the other quantity. The comparison between Figures 2, 4 and 5 support this inference. To characterize the impact of this on our determination of the saturation points, we have mapped each $\lvert\delta n_H/n_H\rvert$ quantile to $\lvert\sigma_c\rvert$ using both v_s and A_s. We refer to this as "mapped $\lvert\sigma_c\rvert$". We similarly mapped each $\lvert\sigma_c\rvert$ quantile from Paper 1 to $\lvert\delta n_H/n_H\rvert$ using both v_s and A_s derived in that work. Here, we derive and present those mappings. We then discuss their implications. Table 5 summarizes mapped $\lvert\sigma_c\rvert$ in each $\lvert\delta n_H/n_H\rvert$ quantile using A_s and v_s. Similarly, Table 6 summarizes mapped $\lvert\delta n_H/n_H\rvert$ in each $\lvert\sigma_c\rvert$ quantile. These mappings and their implications serve to confirm the results presented in the main portion of this work.

3.8.1. *Mapping Quantiles of $\lvert\delta n_H/n_H\rvert$ to $\lvert\sigma_c\rvert$ with A_s*

Figure 18 plots the average $\lvert\sigma_c\rvert$ as a function of A_{He} in 0.2% wide bins for each $\lvert\delta n_H/n_H\rvert$ quantile. With this figure, we can map $\lvert\delta n_H/n_H\rvert$ quantiles to $\lvert\sigma_c\rvert$ using A_s. The shaded regions indicate the uncertainty, calculated

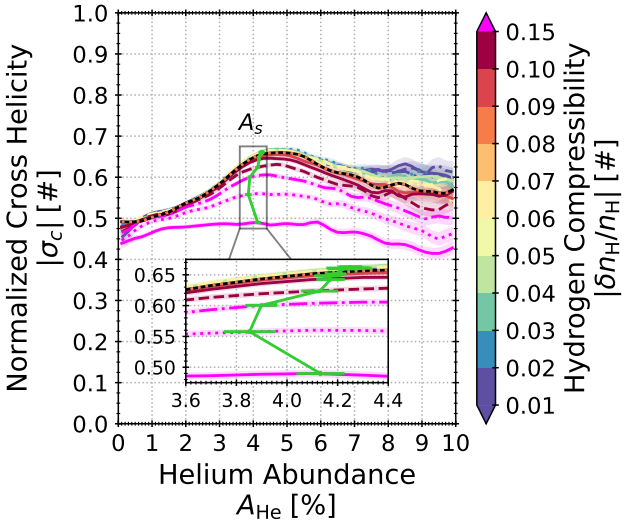

Figure 18. The average normalized cross helicity ($|\sigma_c|$) as a function of the helium abundance (A_{He}) in each of 15 compressibility ($|\delta n_H/n_H|$) quantiles. Shaded regions indicate the standard error of the mean. The color of each $|\delta n_H/n_H|$ quantile is given by the color bar. Lines are smoothed with a 1σ Gaussian filter for visual clarity. Compressibilities $|\delta n_H/n_H| > 0.15$ are plotted in pink. The quantile corresponding to $|\delta n_H/n_H| = 0.085$ is highlighted by plotting the dotted orange line on top of a black solid line. The green line plots A_s ($|\sigma_c|$) in each $|\delta n_H/n_H|$ quantile.

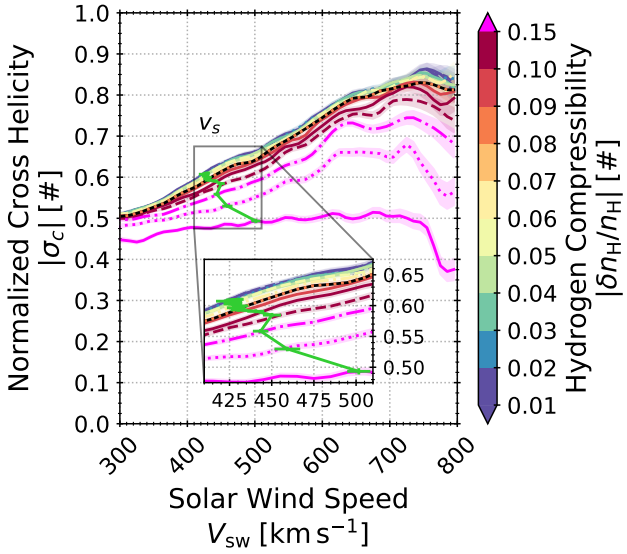

Figure 19. The normalized cross helicity as a function of v_{sw} in the 15 $|\delta n_H/n_H|$ quantiles. Style matches Figure 18, with the green line indicating v_s instead of A_s.

as the standard error of the mean (SEM). Lines and uncertainties are smoothed with a 1σ Gaussian filter for visual clarity. The $|\delta n_H/n_H|$ quantiles are given by the color bar and the line styles vary across quantiles. The line for the quantile in which $|\delta n_H/n_H| = 0.085$ is over plotted on a black line to highlight it. As in prior figures, quantiles with $|\delta n_H/n_H| > 0.15$ are plotted in pink. The green line indicates $|\sigma_c|$ at A_s in each $|\delta n_H/n_H|$ quantile. The inset axis enlarges the region surrounding A_s. We make the following observations in Figure 18.

1. $|\sigma_c|$ increases with A_{He} in all but the most compressive $|\delta n_H/n_H|$ quantile, reaching a maximum at $\gtrsim A_s$ and then decreasing as A_{He} increases.
2. For incompressible quantiles ($|\delta n_H/n_H| < 0.15$), we observe the following:
   (a) $|\sigma_c|\,(A_{He}, |\delta n_H/n_H|)$ is independent of $|\delta n_H/n_H|$ for $A_{He} < A_s$.
   (b) As A_{He} increases to values greater than A_s, $|\sigma_c|$ depends on $|\delta n_H/n_H|$ and the spread in $|\sigma_c|$ increases with increasing $|\delta n_H/n_H|$.
   (c) The dependence of average $|\sigma_c|$ on A_{He} for $A_{He} > A_s$ decreases with decreasing $|\delta n_H/n_H|$.
3. For compressible quantiles ($|\delta n_H/n_H| > 0.15$), we observe the following:
   (a) The overall dependence of $|\sigma_c|$ on A_{He} decreases with decreasing $|\delta n_H/n_H|$.
   (b) For the most compressible solar wind (largest $|\delta n_H/n_H|$), average $|\sigma_c|$ is just smaller than 0.5 over the range $A_{He} \approx 1$ to $\sim 6\%$. For $A_{He} > 6\%$, even $|\sigma_c|$ in the most compressible solar wind decreases with increasing A_{He}.
4. The gradients of $|\sigma_c|\,(A_{He}, |\delta n_H/n_H|)$ are steeper for $A_{He} < A_s$ than for $A_{He} > A_s$.

In other words, at low A_{He}, all $|\delta n_H/n_H|$ map to $|\sigma_c| \sim 0.5$ and the possible values of $|\sigma_c|$ at any given $(A_{He}, |\delta n_H/n_H|)$ increases as A_{He} increases.

3.8.2. *Mapping Quantiles of $|\delta n_H/n_H|$ to $|\sigma_c|$ with v_s*

Figure 19 allows us to apply the same method in Figure 18 to mapping $|\delta n_H/n_H|$ quantiles to $|\sigma_c|$ using v_s. Here, we use v_{sw} bins that are 10 km s^{-1} wide. The figure style matches Figure 18. Here, the green line indicates v_s and the inset axis highlights the region surrounding it. We make the following observations.

1. The dependence of average $|\sigma_c|$ on v_{sw} becomes weaker as $|\delta n_H/n_H|$ increases.
2. For incompressible solar wind with $|\delta n_H/n_H| < 0.15$, there is a strong, monotonic increase of $|\sigma_c|$ with increasing v_{sw} up to ~ 750 km s^{-1}. The value of average $|\sigma_c|$ in this range of speeds only weakly depends on $|\delta n_H/n_H|$ for any given v_{sw}. At speeds above ~ 750 km s^{-1}, $|\sigma_c|$ decreases with increasing

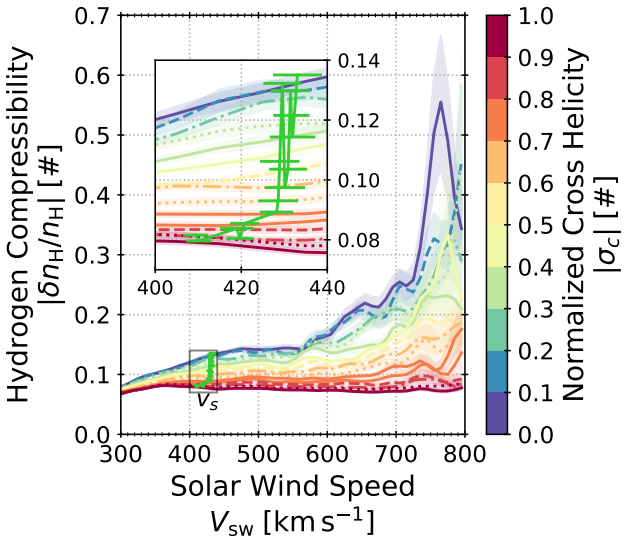

Figure 20. The hydrogen compressibility $|\delta n_H/n_H|$ as a function of the solar wind speed v_{sw} in quantiles of $|\sigma_c|$, which is given by the colorbar. The green line labeled v_s indicates $|\delta n_H/n_H|$ in each $|\sigma_c|$ quantile at the corresponding saturation abundance.

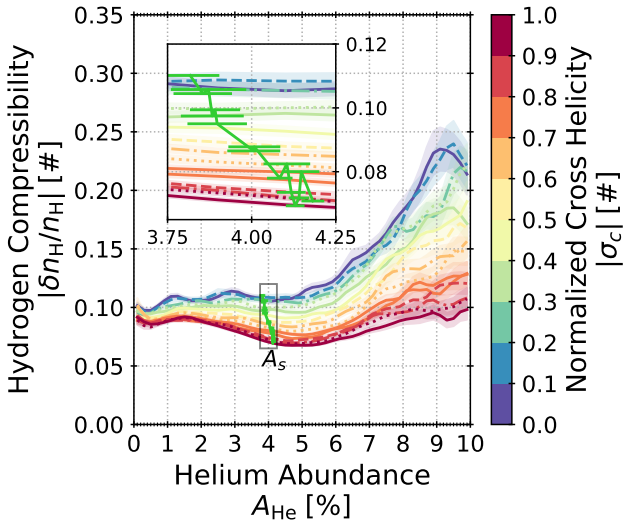

Figure 21. The hydrogen compressibility $|\delta n_H/n_H|$ as a function of the helium abundance A_{He} in quantiles of $|\sigma_c|$, which is given by the colorbar. The green line labeled A_s indicates $|\delta n_H/n_H|$ in each $|\sigma_c|$ quantile at the corresponding saturation abundance.

v_{sw}. Due to the low frequency at which solar wind speeds of this range are observed, we do not draw an inference about $|\sigma_c|$ in these fastest speeds.

3. Incompressible solar wind with $|\delta n_H/n_H| > 0.15$, the dependence of $|\sigma_c|$ on $|\delta n_H/n_H|$ for any given v_{sw} is markedly stronger, while $|\sigma_c|$ strongly depends on v_{sw} in the compressible quantile with the smallest $|\delta n_H/n_H|$. For the solar wind in the most compressive $|\delta n_H/n_H|$ quantile, $|\sigma_c|$ is almost independent of speed.

Similar to the A_s mapping in Figure 18, $|\delta n_H/n_H|$ in slow wind maps to $|\sigma_c| \sim 0.5$, while it maps to a large range $|\sigma_c|$ in fast wind and the range increases with $|\delta n_H/n_H|$.

3.8.3. *Mapping Quantiles of $|\sigma_c|$ to $|\delta n_H/n_H|$ with v_s*

To fully compare the results in Paper 1 across $|\sigma_c|$ quantiles and those presented in this paper across $|\delta n_H/n_H|$ quantiles, Figures 20 and 21 apply the technique in the previous section generate the inverse mapping from $|\sigma_c|$ in each of 15 quantiles at the saturation point to $|\delta n_H/n_H|$. The insert in each figure zooms in on the boxed region surrounding the appropriate saturation quantity (v_s or A_s).

Figure 20 plots $|\delta n_H/n_H|\,(v_{sw})$ for each $|\sigma_c|$ quantile. From it, we make the following observations.

1. In Alfvénic wind with $|\sigma_c| \gtrsim 0.7$, the compressibility is approximately constant with $|\delta n_H/n_H| < 0.09$ for all but the fastest speeds with $v_{sw} \lesssim 750$ km s^{-1}, above which $|\delta n_H/n_H|$ increases by increasing amounts as $|\sigma_c|$ increases. $|\delta n_H/n_H|$ increases markedly above 0.3 in the fastest wind.
2. The insert shows that v_s is approximately independent of $|\delta n_H/n_H|$ when $|\delta n_H/n_H| > 0.09$.
3. In the slowest wind, $|\delta n_H/n_H| < 0.1$ across $|\sigma_c|$.

That $|\delta n_H/n_H|$ increases with increasing $v_{sw} > 560$ km s^{-1}, the magnitude of the increase is larger with in non-Alfvénic solar wind, and $v_{sw} > v_s$ is observed across all $|\delta n_H/n_H|$ in Figure 16, reinforces the observation made throughout this paper that v_{sw} does not uniquely map to either non-Alfvénic, compressible or Alfvénic, incompressible solar wind. Rather there is a wide range of speeds for both types of plasmas.

3.8.4. *Mapping Quantiles of $|\sigma_c|$ to $|\delta n_H/n_H|$ with A_s*

Figure 21 plots $|\delta n_H/n_H|\,(A_{He})$ for each $|\sigma_c|$ quantile. The range of $|\delta n_H/n_H|$ values in this figure is half as large as the range in Figure 20 so that the variability in the plot is readable. The green markers indicate the compressibility $|\delta n_H/n_H|$ at A_s in each $|\sigma_c|$ quantile, which is labeled with A_s on the plot. The insert axis zooms in on the indicated region surrounding A_s. From this figure, we make the following observations.

1. As A_{He} approaches 0, the compressibility $|\delta n_H/n_H| \sim 0.1$ is approximately constant across $|\sigma_c|$.
2. For abundances $A_{He} \lesssim 5\%$, $|\delta n_H/n_H|$ decreases with increasing A_{He} in Alfvénic wind and is approximately constant for non-Alfvénic wind.

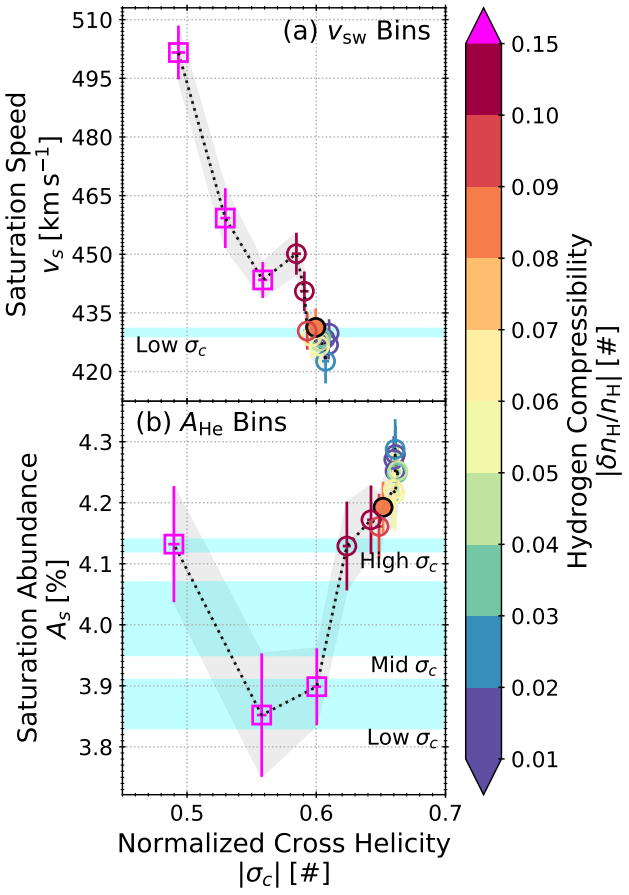

Figure 22. The saturation point (v_s, A_s) in Figure 11 plotted as a function of $|\sigma_c|$. Points are connected by a dotted line to aid the eye. Uncertainties are plotted as error bars with the same color as the markers and a semi-transparent gray envelope traces out the envelope surrounding the error bars. Each $|\delta n_H/n_H|$ quantiles is mapped to $|\sigma_c|$ using (a) Figure 19 and (b) Figure 18. Markers excluding the quantile $|\delta n_H/n_H| = 0.085$ are unfilled. The $|\delta n_H/n_H| = 0.085$ quantile marker is filled and has a black edge. As in Figure 11, the blue horizontal regions correspond to average value of (a) v_s and (b) A_{He} for key ranges of $|\sigma_c|$ derived in Paper 1.

3. For abundances $A_{He} \gtrsim 5\%$, the minimum compressibility is
   (a) is $|\delta n_H/n_H| = 0.067$,
   (b) reaches this minimum at $A_{He} \approx 5.3\%$, and
   (c) $|\delta n_H/n_H|$ is smallest for the largest $|\sigma_c|$,
4. At $A_{He} \gtrsim 5.3\%$, $|\delta n_H/n_H|$ increases across all $|\sigma_c|$ and the gradient of $|\delta n_H/n_H|$ as a function of A_{He} increases with decreasing $|\sigma_c|$ such that $|\delta n_H/n_H|$ takes on its largest range of values at the largest A_{He}. In particular,
   (a) In Alfvénic wind with large $|\sigma_c|$, $|\delta n_H/n_H|$ tends towards the same 10% observed with vanishingly small A_{He}.
   (b) In non-Alfvénic wind with small $|\sigma_c|$, the compressibility tends towards $|\delta n_H/n_H| > 0.20$. the maximum $|\sigma_c|$ in Alfvénic subset of enhanced A_{He} (Figure 15).

Similar to the observations in Figure 20, we observe a larger gradient of $|\delta n_H/n_H|$ across $|\sigma_c|$ as A_{He} increases. Although the maximum $|\delta n_H/n_H|$ in the largest A_{He} is $\sim 2x$ smaller than the maximum $|\delta n_H/n_H|$ in the fastest v_{sw}, the anti-correlation between $|\delta n_H/n_H|$ and $|\sigma_c|$ is still recovered as A_{He} increases.

3.9. *Mapping between the dependence of (v_s, A_s) and the saturation slope on $|\delta n_H/n_H|$ and $|\sigma_c|$*

Using the relationships derived in Sections 3.8.1 to 3.8.4, we can map the dependence of the saturation point (v_s, A_s) along with the saturation slope from $|\delta n_H/n_H|$ to $|\sigma_c|$. While much of this can be observed combining the mappings with observations in Section 3, it is presented here for completeness. Figure 22 plots the dependence of the saturation point derived in $|\delta n_H/n_H|$ quantiles as a function of mapped $|\sigma_c|$. Panel (a) plots v_s ($|\sigma_c|$). Here, we derive $|\sigma_c|$ from Figure 19 and calculate the mean $|\sigma_c|$ in each $|\delta n_H/n_H|$ quantile for the v_{sw} bin in which v_s falls. This is what "v_{sw} Bins" next to the panel label indicates. Panel (b) plots A_s ($|\sigma_c|$), applying the same mapping method using Figure 18 to determine the mean $|\sigma_c|$ in each $|\delta n_H/n_H|$ quantile for the A_{He} bin in which A_s falls. The figure style follows Figure 11, including the $|\sigma_c|$ ranges from Paper 1 highlighted with blue bars. The major change in style is that markers are unfilled, with the exception of the $|\delta n_H/n_H| = 0.085$ quantile, which is filled and has a black edge. We make the following observations in Panel (a) regarding the mapping using v_s.

1. Incompressible solar wind mapped to $|\sigma_c|$ with v_s has $|\sigma_c| \approx 0.6$.
2. Compressible solar wind mapped to $|\sigma_c|$ with v_s has $|\sigma_c| < 0.06$.

In Panel (b), we observe the following about the mapping using A_s.

1. Incompressible solar wind mapped to $|\sigma_c|$ using A_s has $|\sigma_c| \approx 0.65$.
2. Compressible solar wind happed to $|\sigma_c|$ using A_s has $|\sigma_c| \lesssim 0.6$.

Comparing Panels (a) and (b), we observe that the minimum mapped $|\sigma_c|$ is approximately the same when mapped $|\sigma_c|$ is derived for v_s and for A_s. In contrast, the maximum mapped $|\sigma_c|$ is larger when derived for A_s than when derived for v_s.

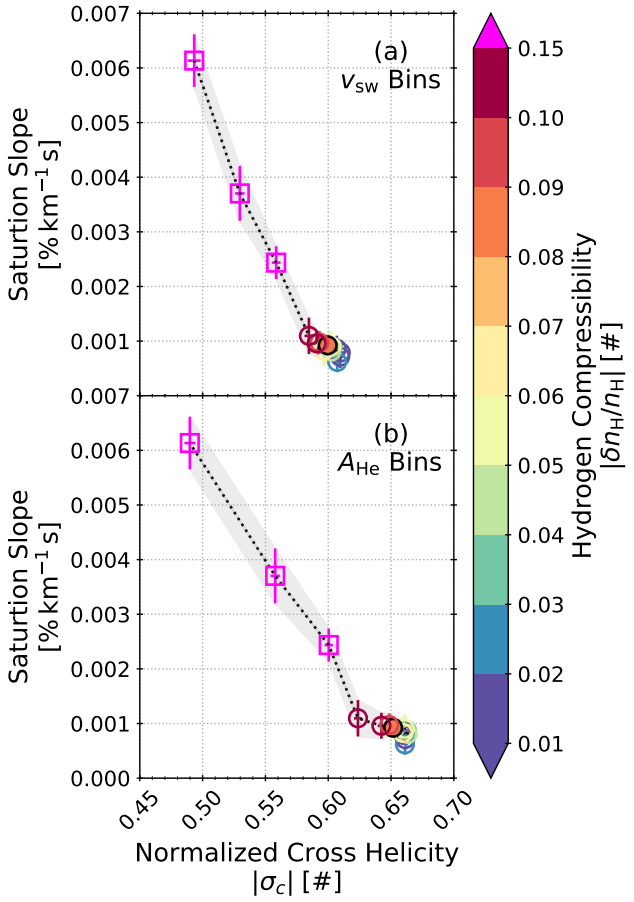

Figure 23. The saturation slopes from Figure 12 as a function of $|\sigma_c|$. In panel (a), $|\delta n_H/n_H|$ in Figure 12 is mapped to $|\sigma_c|$ using the trends in Figure 19 by calculating the $|\sigma_c|$ corresponding to v_s in each $|\delta n_H/n_H|$ quantile. We then plot the saturations slope in that $|\delta n_H/n_H|$ quantile as a function of this $|\sigma_c|$. In panel (b), we use the same method and determining the $|\sigma_c|$ corresponding to A_s in each $|\delta n_H/n_H|$ quantile from Figure 18. Because markers corresponding to $|\delta n_H/n_H| \leq 0.085$ overlap, markers are unfilled. The exception are markers corresponding to the $|\delta n_H/n_H| = 0.085$ level, which are filled.

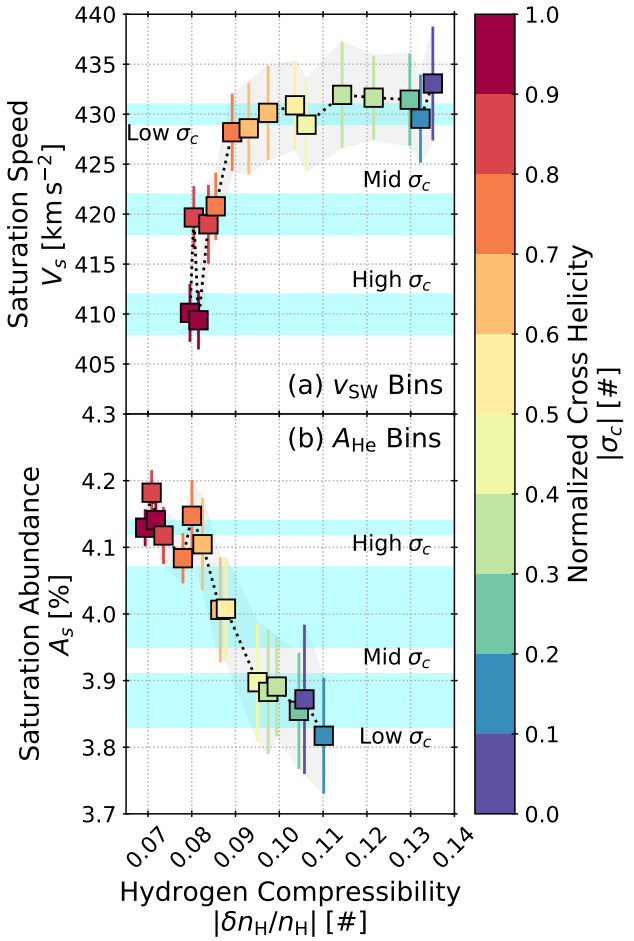

Figure 24. The saturation **(a)** speed v_s and **(b)** abundance A_s as a function of compressibility $|\delta n_H/n_H|$ for each $|\sigma_c|$ quantile, which is given by the color bar. Points are connected by a dotted line to aid the eye. Uncertainties are plotted as error bars with the same color as the markers and a semi-transparent gray envelope traces out the envelope surrounding the error bars. This figure is similar to Figure 22 in that it maps $|\sigma_c|$ for each saturation point derived in Paper 1 to $|\delta n_H/n_H|$ in its $|\sigma_c|$ quantile. In effect, it is the analagous mapping in Figure 22 for Paper 1, Figure 6

Figure 23 applies the same mapping techniques in Figure 22 to the saturation slope in Figure 12 using both (a) v_s and (b) A_s. The figure style matches Figure 22. As expected, compressible slopes mapped to $|\sigma_c|$ from $|\delta n_H/n_H|$ with v_s have $|\sigma_c| < 0.575$, while incompressible slopes $\sim 0.001\% \, km^{-1} \, s$ are fixed at a constant $|\sigma_c| = 0.06$. Similarly, compressible slopes mapped to $|\sigma_c|$ from $|\delta n_H/n_H|$ with A_s have $|\sigma_c| \lesssim 0.6$, while incompressible slopes map to $|\sigma_c| \approx 0.65$.

Broadly, Figures 22 and 23 imply that less compressible solar wind is more Alfvénic it is and the less compressible it is, the less A_{He} departs from A_s. However, it also confirms that the average cross helicity or Alfvénicity in any incompressible $|\delta n_H/n_H|$ quantile tends towards $|\sigma_c| \sim 0.6$, which is the value in Figure 6 at which we observe saturation, and does not reflect the full range of Alfvénic solar wind.

Figure 24 plots (a) the saturation speed v_s and (b) the saturation abundance A_s as a function of mapped $|\delta n_H/n_H|$. The general style matches Figures 22 and 23. The exception is that $|\delta n_H/n_H|$ and $|\sigma_c|$ are swapped. The color bar now indicates $|\sigma_c|$ and v_s and A_s are now plotted as a function of mapped $|\delta n_H/n_H|$. The blue

bands are distinct ranges of $|\sigma_c|$ defined in Paper 1. We observe the following observations about v_s.

1. The mid and high $|\sigma_c|$ subsets defined in Paper 1 are grouped tightly into mapped $|\delta n_H/n_H|$ corresponding to $|\delta n_H/n_H| \lesssim 0.085$.
2. The low $|\sigma_c|$ range of v_s extends to higher mapped $|\delta n_H/n_H|$.

From Panel (b), we observe the following about A_s.

1. The dependence of A_s on mapped $|\delta n_H/n_H|$ is roughly linear. Fitting the observations of A_s as a function of mapped $|\delta n_H/n_H|$ with a line yields a slope of $-8.6 \pm 0.5\%/\#$ and a y-intercept of $A_s = 4.76 \pm 0.04\%$, i.e. A_s in perfectly incompressible solar wind.
2. Again, the mid $|\sigma_c|$ subset is tightly clustered. The low and high $|\sigma_c|$ subsets are less clustered.

Comparing mapped $|\delta n_H/n_H|$ derived in both panels, we observe the following.

1. Neither v_s nor A_s are observed at a mapped $|\delta n_H/n_H|$ corresponding to incompressible $|\delta n_H/n_H| > 0.15$.
2. The minimum and maximum mapped $|\delta n_H/n_H|$ is smaller when derived for A_s than when derived for v_s, but does not reach the lowest $|\delta n_H/n_H| \approx 0.01$ observed in Figures 11 and 12.

This mapping shows that incompressible $|\delta n_H/n_H|$ is dominant across $|\sigma_c|$, but this value depends how the solar wind observations are aggregated.

4. DISCUSSION

The saturation abundance A_s is $49 \pm 2\%$ of the photospheric abundance. Alterman et al. (2025, Figure 1) show that the the helium abundance above saturation oscillates around $51 \pm 3\%$ of the photospheric helium abundance across solar activity, while the helium abundance below saturation only reaches a maximum of this value during solar maxima. These observations suggest that this factor of 2 depletion of solar wind A_{He} from its photospheric value is robust across solar activity as the heliographic latitude of open and closed source regions evolve with the solar cycle.

Paper 1 shows that $\nabla_{v_{sw}} A_{He}$ for speeds $v_{sw} > v_s$ increase with decreasing $|\sigma_c|$. Figure 25 plots $A_{He}\left(v_{sw} = 800\ \mathrm{km\,s^{-1}}\right)$, the helium abundance in each $|\sigma_c|$ quantile from Paper 1 at the fastest analyzed speed ($v_{sw} = 800\ \mathrm{km\,s^{-1}}$) normalized to A_s in that quantile. In the most Alfvénic solar wind, A_{He} is enhanced by $\sim 10\%$ with respect to A_s. In the least Alfvénic solar wind, A_{He} is enhanced by $\sim 40\%$. The enhancement of A_{He} above A_s decreases linearly with increasing $|\sigma_c|$. The dash-dotted line is a fit to the trend with a slope of -0.4 ± 0.02 and a y-intercept of 1.46 ± 0.02, indicating

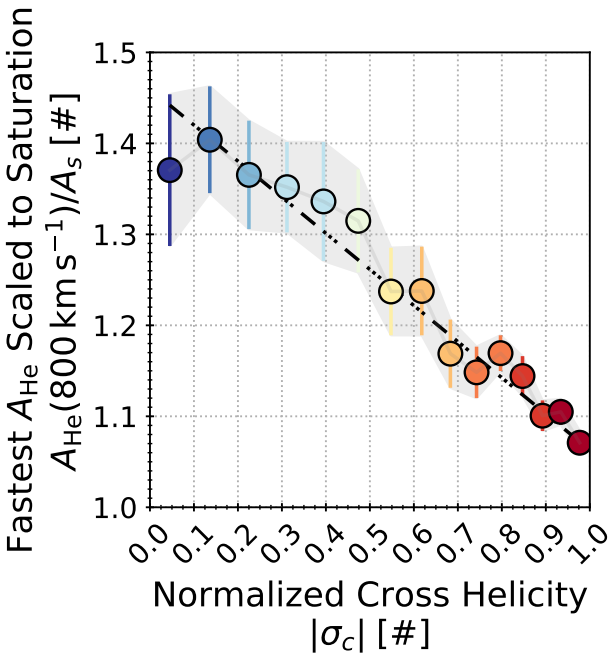

Figure 25. Helium abundance at $800\ \mathrm{km\,s^{-1}}$ derived from the fits of $A_{He}(v_{sw})$ across $|\sigma_c|$ quantiles in Paper 1, each scaled to the saturation abundance A_s in that paper. Error bars and markers are colored by $|\sigma_c|$ to facilitate comparison with prior figures. The dash-dotted line is a fit to the trend.

that A_{He} in the fastest wind would be 46% larger than A_s in perfectly non-Alfvénic and therefore compressible solar wind. As $v_{sw} > v_s$ is nominally from magnetically open sources and such solar wind is typically Alfvénic and incompressible, this seems to suggest that A_{He} is not limited to $\sim 50\%$ of its photospheric value, contradicting Alterman et al. (2025).

We have combined the helium abundance with the normalized cross helicity and solar wind compressibility to address this apparent contradiction. We observe that $|\delta n_H/n_H| \lesssim 0.85$ in the (v_{sw}, A_{He})-plane where A_{He} observations are most common. This suggests that $|\delta n_H/n_H|$ may regulate A_{He} in the solar wind. To verify this inference, we have performed the following analysis.

1. Comparing $|\delta n_H/n_H|\,(v_{sw}, A_{He})$ with the saturation fits derived in Paper 1.
2. Analyzing helium saturation as a function of v_{sw} across 15 $|\delta n_H/n_H|$ quantiles.
3. Repeating Paper 1's analysis selecting for $|\delta n_H/n_H| < 0.085$, 0.1, and 0.15 along with $|\delta n_H/n_H| > 0.15$.
4. Characterizing v_{sw} and A_{He} in the $(|\sigma_c|, |\delta n_H/n_H|)$-plane.
5. Characterizing $|\delta n_H/n_H|$ in the $(|\sigma_c|, A_{He})$-plane, which Paper 1 uses to identify solar wind observa-

tions predominantly from magnetically open and closed source regions.

6. Mapping saturation points derived in quantiles of $|\delta n_{\rm H}/n_{\rm H}|$ or $|\sigma_c|$ to the other quantity.

We have also visualized the saturation speeds derived here with other key speeds derived by Paper 1, Alterman et al. (2024), and Alterman (2025) in the bimodal distribution of speeds observed near-Earth during solar minima.

4.1. $|\delta n_{\rm H}/n_{\rm H}|\,(v_{\rm sw}, A_{\rm He})$ and the Saturation Fits in Paper 1

Comparing $|\delta n_{\rm H}/n_{\rm H}|\,(v_{\rm sw}, A_{\rm He})$ with the saturation fits derived in Paper 1 reveals the following.

1. The central values and standard deviation of $A_{\rm He}$ across $v_{\rm sw}$ are roughly limited to the incompressible region of the $(A_{\rm He}, v_{\rm sw})$-plane where $|\delta n_{\rm H}/n_{\rm H}| < 0.1$. This is below the range of compressibilities observed by Probe below 139.64 R_S Adhikari et al. (2020).
2. Above saturation, $A_{\rm He}$ in non-Alfvénic solar wind exceeds $A_{\rm He}$ in Alfvénic solar wind over the range of speeds $v_{\rm sw} = 530$ to 560 km s^{-1}, which corresponds to the same region where $|\sigma_c|\,(A_{\rm He}, v_{\rm sw}) = 0.7$ in Figure 6. $|\sigma_c| = 0.68$ is the lower bound on the Alfvénic subset defined in Paper 1 based on A_s. This speed range is below $v_{\rm fast}$ defined in Paper 1, where the frequency of speed observations has dropped significantly from the slow wind peak and where solar wind observed at 1 AU predominantly originates in open field regions, and v_K. $v_{\rm fast}$ is the peak of the fast wind distribution and v_K is the speed predicted at 1 AU from the radial scaling of the kinetic energy flux observed with Probe near-Sun observations (Liu et al. 2021). This range of speeds also falls within the range v_{IP}, which Alterman (2025) identifies as solar wind from source regions that typically generate fast wind, but is Alfvén wave-poor in that the energy in the Alfvénic fluctuations is reduced in comparison to typical fast wind and is therefore not accelerated to the fastest, non-transient speeds observed near Earth.
3. The solar wind's compressibility increases with increasing $A_{\rm He}$ and $v_{\rm sw}$, which are observed less frequently at 1 AU than slower speeds and lower $A_{\rm He}$.

These suggest that the increase of $\nabla_{v_{\rm sw}} A_{\rm He}$ with decreasing $|\sigma_c|$ at speeds above saturation ($v_{\rm sw} > v_s$) are related to the presence of compressive fluctuations, which are a significant fraction of the observations in this region of parameter space where observations are less frequent.

4.2. $A_{\rm He}\,(v_{\rm sw})$ Saturation Fits Across $|\delta n_{\rm H}/n_{\rm H}|$ Quantiles and Repeating Paper 1's Analysis Across $|\sigma_c|$ Quantiles for Incompressible and Compressible Subsets

Analyzing helium saturation as a function of $v_{\rm sw}$ across 15 quantiles of $|\delta n_{\rm H}/n_{\rm H}|$ shows that the large $\nabla_{v_{\rm sw}} A_{\rm He}$ above saturation are limited to compressible solar wind with $|\delta n_{\rm H}/n_{\rm H}| > 0.15$, while $\nabla_{v_{\rm sw}} A_{\rm He}$ in incompressible solar wind is virtually indistinguishable. Repeating the analysis from Paper 1 for incompressible subsets of our observations with $|\delta n_{\rm H}/n_{\rm H}| < 0.085$, 0.1, 0.15; the compressible subset with $|\delta n_{\rm H}/n_{\rm H}| > 0.15$; and the results in Paper 1 derived without regard to $|\delta n_{\rm H}/n_{\rm H}|$ shows that v_s, A_s, and m_s for any of the incompressible thresholds are similar and are also similar to the values derived irrespective of compressibility. This suggests that the overall behavior of $A_{\rm He}\,(v_{\rm sw})$ across $|\sigma_c|$ is dominated by incompressible solar wind and that compressive fluctuations across $|\sigma_c|$ drive the large $\nabla_{v_{\rm sw}} A_{\rm He}$ for speeds $v_{\rm sw} > v_s$. It also suggests that the incompressible results are not sensitive to a threshold chosen below $|\delta n_{\rm H}/n_{\rm H}| = 0.015$.

Comparing v_s and A_s derived across $|\sigma_c|$ and $|\delta n_{\rm H}/n_{\rm H}|$ quantiles reveals

1. $v_s = 428 \pm 1.4$ km s^{-1} in incompressible solar wind doesn't exceed the largest $v_s = 430$ km s^{-1} in Paper 1. This largest v_s in Paper 1 corresponds to non-Alfvénic solar wind.
2. v_s in compressive solar wind reaches speeds 17% larger than non-Alfvénic $v_s = 430$ km s^{-1} from Paper 1.
3. Excluding the largest $|\delta n_{\rm H}/n_{\rm H}|$ quantile, compressible A_s is within the range of non-Alfvénic A_s derived in Paper 1.
4. Incompressible A_s only drop to Alfvénic A_s at the largest incompressible $|\delta n_{\rm H}/n_{\rm H}|$.
5. The saturation slopes are fixed at $\sim 10^{-3}$ for incompressible $|\delta n_{\rm H}/n_{\rm H}|$ and jumps by $> 6\times$ in the most compressible $|\delta n_{\rm H}/n_{\rm H}|$.

This substantiates the broad observation in Figures 2 and 4 that compressive fluctuations are present across $|\sigma_c|$ when $|\sigma_c|$ is plotted as a function of $v_{\rm sw}$. We infer that these compressive fluctuations impact the saturation points derived in Paper 1 and lead to the apparent paradox in Sections 3.1 and 3.2.

4.3. $A_{\rm He}$ and $v_{\rm sw}$ in the $(|\sigma_c|, |\delta n_{\rm H}/n_{\rm H}|)$-Plane

Characterizing $A_{\rm He}$ in the $(|\sigma_c|, |\delta n_{\rm H}/n_{\rm H}|)$-plane shows that:

1. Helium-rich solar wind with $A_{\rm He} > A_s$ can be both compressible and incompressible.

2. $A_{\rm He} > A_s$ in the the compressible subset reaches $A_{\rm He}$ in excess of 7.5% and is highly variable. This subset does not have a preferred $|\sigma_c|$.
3. Excluding a trivial region, $A_{\rm He} > A_s$ in the incompressible subset does not exceed 6% and displays very little variability. This subset has $|\delta n_{\rm H}/n_{\rm H}| \lesssim 0.2$. While this threshold is larger than any defined previously, only a small fraction of the enhanced $A_{\rm He}$ in this Alfvénic region of the plane reach this compressibility. As such, averages in $|\delta n_{\rm H}/n_{\rm H}|$ or $|\sigma_c|$ quantiles likely obscure this small fraction of the observations.

The presence of $A_{\rm He} > A_s$ that is highly variable across $|\sigma_c|$ at high $|\delta n_{\rm H}/n_{\rm H}|$ further implies that a non-trivial subset of solar wind has an enhanced $A_{\rm He}$ due to compressive fluctuations. From this, we infer that the enhancement of $\nabla_{v_{\rm sw}} A_{\rm He}$ for speeds $v_{\rm sw} > v_s$ is due to compressive fluctuations in Alfvénic solar wind. This is supported by Figures 4 and 5, which show that $|\delta n_{\rm H}/n_{\rm H}| > 0.1$ is present across speeds $v_{\rm sw} \gtrsim 300$ km s^{-1} and compressive fluctuations become more significant at higher $v_{\rm sw}$ with low $|\sigma_c|$.

Characterizing $v_{\rm sw}$ in the $(|\sigma_c|, |\delta n_{\rm H}/n_{\rm H}|)$-plane shows that Alfvénic solar wind has faster average speeds and smaller variability than compressive solar wind across $|\sigma_c|$. In particular,

1. the average $v_{\rm sw}$ in the incompressible subset exceeds the largest v_s observed in the incompressible $|\delta n_{\rm H}/n_{\rm H}| = 0.143$ quantile.
2. $v_s = 430$ km s^{-1} from the non-Alfvénic solar wind in Paper 1, which is slower than $v_{\rm sw}$ in the incompressible subset, falls within the range of $v_{\rm sw}$ in the compressive subset.
3. The variability of $v_{\rm sw}$ in the incompressible subset is larger than the variability in the incompressible subset.
4. The expected anti-correlation between $|\delta n_{\rm H}/n_{\rm H}|$ and $|\sigma_c|$ is recovered across contours of constant $v_{\rm sw}$, even though $v_{\rm sw}$ is highly variable, suggesting that a wide range of $v_{\rm sw}$ are observed in incompressible, Alfvénic and compressible, non-Alfvénic solar wind and these speed ranges significantly overlap.

Together, these imply that the compressibility is driving changes in $A_{\rm He}$, not changes in $v_{\rm sw}$ itself. They also confirm that the overlap in $v_{\rm sw}$ corresponding to incompressible, Alfvénic and compressible, non-Alfvénic solar wind leads to the apparent paradox in Sections 3.1 and 3.2.

The comparison between $A_{\rm He}$ and $v_{\rm sw}$ in the $(|\sigma_c|, |\delta n_{\rm H}/n_{\rm H}|)$-plane suggests that the enhancement in $A_{\rm He}$ is not limited to fast solar wind, typically considered to have originated in continuously open field source regions. Rather, there also exists a subset of solar wind with an enhanced and highly variable $A_{\rm He} > A_s$ where the compressibility is large, the average $v_{\rm sw}$ does not exceed v_s for the compressible subset ($v_{\delta n'}$ in Figure 14), and $v_{\rm sw}$ is less variable than in the Alfvénic subset. This suggests that enhanced $A_{\rm He} > A_s$ is not limited to solar wind from continuously open sources on the Sun, in agreement with Alterman et al. (2025).

4.4. $|\delta n_{\rm H}/n_{\rm H}|$ *in the* $(|\sigma_c|, A_{\rm He})$*-Plane*

Paper 1 shows that solar wind from closed and open source regions can be separated into different regions of the $(|\sigma_c|, A_{\rm He})$-plane. Characterizing $|\delta n_{\rm H}/n_{\rm H}|$ in this plane shows that:

1. compressible solar wind with $|\delta n_{\rm H}/n_{\rm H}| > 0.15$ is limited to non-Alfvénic, helium-rich solar wind,
2. incompressible solar wind with $|\delta n_{\rm H}/n_{\rm H}| < 0.85$ is limited to $2.5\% \lesssim A_{\rm He} \lesssim 7.5\%$,
3. and this incompressible range corresponds to the region of the $(|\sigma_c|, A_{\rm He})$-plane with solar wind from magnetically open source regions.

In other words, solar wind is least compressible in the region of the plane that Paper 1 identifies as solar wind from open sources like coronal holes and compressive solar wind is limited the region of the plane where $A_{\rm He}$ is more than 1.4× larger than the largest A_s. From this, we infer that the compressive subset is of unique origin with a source region not traditionally considered to be continuously or intermittently magnetically open. Ongoing work suggest that this subset of observations corresponds to transients.

4.5. *The Bimodal Distribution of Speeds Observed Near Earth During Solar Minima*

Paper 1 visualizes the key speeds derived in that work on the distribution of $v_{\rm sw}$ observed during solar minima. To this distribution, Figure 14 adds the speeds $v_{\delta n}$, $v_{\delta n'}$, $v_{\rm heavy}$ (Alterman et al. 2024), v_{IP} (Alterman 2025), and v_K (Alterman 2025).

1. The range of incompressible v_s ($v_{\delta n}$) falls within the full range of v_σ and the faster portion of v_n. v_σ is the range of saturation speeds in Paper 1 and v_n is the range of speeds over which $n_{\rm He}$ ($v_{\rm sw}$) reaches a local maximum. This local maximum is indicative of how He's role in solar wind at the sonic point changes between continuously and intermittently open source regions (Paper 1; Lie-Svendsen et al. 2001; Lie-Svendsen et al. 2002; Endeve et al. 2005; Lie-Svendsen et al. 2003; Hansteen et al. 1997).
2. The range of compressible v_s ($v_{\delta n'}$) marginally overlaps the fastest portion of v_σ and is within

the range of speeds v_{IP}, which corresponds to Alfvén wave-poor solar wind from continuously open source regions with reduced energy in the Alfvénic fluctuations.

3. That $v_{\rm heavy}$ coincides with the slow portion of $v_{\rm slow}$ speed range, effectively at speeds slower than the peak of the $v_{\rm sw}$ distribution, suggests that the processes that lead to the observed helium saturation speeds (which necessarily increases during transit through interplanetary space due to in-transit acceleration) do not impact heavier elements in the same manner (Alterman et al. 2024).
4. The range of speeds v_{IP}, overlaps with v_σ, $v_{\delta n}$, and $v_{\delta n'}$, reaching a maximum value just greater than the minimum $v_{\rm fast}$ and v_K.
5. The range of speeds over which non-Alfvénic $A_{\rm He}$ above saturation ($v_{\rm sw} > v_s$) becomes larger than Alfvénic $A_{\rm He}$ above saturation is $530-560$ km s^{-1} (Figure 8), which sits within the v_{IP} range above $v_{\delta n'}$ and below $v_{\rm fast}$and v_K.

This suggests that the transition in observations from slow to fast wind at 1 AU is dominated by incompressible and Alfvénic solar wind, but compressive solar wind is significant in intermediate speed range v_{IP}, where *ad hoc* thresholds for the separation between slow and fast wind have often been set (Schwenn 2006; Fu et al. 2018) and likely corresponds to Alfvénic slow wind (Marsch et al. 1981; D'Amicis et al. 2011).

4.6. *Relevance for Source Regions, Pressure Balanced Structures, Slow Modes*

Fully ionized hydrogen constitutes approximately 95% of the solar wind ions. As such, it is typically assumed that the energy carried by helium and heavier elements can be neglected or can be treated as a fixed value. For example, this is common practice in deriving of marginal stability thresholds (e.g. Verscharen et al. 2016). In ambient solar wind, fully ionized helium constitutes around 4.19% to 4.25% of the ionized hydrogen density, corresponding to approximately 17% of the solar wind mass density.

The solar wind's compressibility may also be related to properties of the solar wind's source region on the Sun (Marsch & Tu 1990; Bruno & Carbone 2013). We have shown that there are two distinct subsets of solar wind that are helium-rich and have distinct compressibilities. We have also shown that there are, effectively, two sets of saturation points: a compressible and an incompressible set. The incompressible subset corresponds to Alfvénic solar wind. The compressible subset does not have a preferred Alfvénicity. The two subsets of helium-rich solar wind may point to two distinct sources of helium-rich solar wind at the Sun, each leading to solar wind with distinct compressibilities. Alterman & D'Amicis (2025b) shows that the incompressible subset corresponds to ambient solar wind and ICMEs drive the increased compressibility in the compressible subset.

NI-MHD suggests that compressible fluctuations are generated by the nonlinear interaction between Alfvén waves propagating along the magnetic field and incompressible fluctuations propagating perpendicular to it (Zank & Matthaeus 1992). PBS and slow modes in the solar wind can both be described in the limit of $k_\perp/k_\parallel \rightarrow \infty$ (Hollweg et al. 2014). MHD predictions for slow modes in the solar wind agree better with observations than their kinetic counter parts (Verscharen et al. 2017) and compressive fluctuations may help maintain the stability of differentially streaming helium by modifying the relevant marginal stability conditions (Zhu et al. 2023). PBS may be related to the more recently identified periodic density structures (PDS) (Kepko et al. 2024; Viall & Vourlidas 2015; Viall et al. 2009), which are considered to be signatures of the solar wind's source regions. The overall regulation of $A_{\rm He}\,(v_{\rm sw})$ by $|\delta n_{\rm H}/n_{\rm H}|$ and the narrower ranges in v_s and A_s when compressive fluctuations are excluded suggest that solar wind helium may play a role in the local evolution of the solar wind in transit that is related to the solar wind's compressibility and that the compressive fluctuations may be driven by a process related to the solar wind's sources.

4.7. *Addressing the Hidden Variable(s)*

The mapping between the saturation analysis as a function of $|\delta n_{\rm H}/n_{\rm H}|$ quantiles to $|\sigma_c|$ reveals the following.

1. The dependence of $|\sigma_c|$ on $A_{\rm He}$ and $v_{\rm sw}$ is weakest when $|\delta n_{\rm H}/n_{\rm H}|$ is largest.
2. Below saturation, $|\sigma_c|\,(A_{\rm He})$ is independent of $|\delta n_{\rm H}/n_{\rm H}|$ in incompressible solar wind and, above saturation, the dependence increases with decreasing $|\delta n_{\rm H}/n_{\rm H}|$.
3. In incompressible solar wind, $|\sigma_c|\,(v_{\rm sw})$ is independent of $|\delta n_{\rm H}/n_{\rm H}|$, but strongly dependent on $|\delta n_{\rm H}/n_{\rm H}|$ in compressible solar wind.
4. Incompressible v_s and A_s each occupy small ranges of mapped $|\sigma_c|$ centered around ~ 0.6 and ~ 0.65, respectively, while compressible v_s and A_s cover a wide range of $|\sigma_c|$.
5. Only the compressible saturation slopes for $|\delta n_{\rm H}/n_{\rm H}| > 0.15$ depart from these two clusters and reach $|\sigma_c|$ smaller than them

From these observations, we infer that there is a critical transition in the range $|\sigma_c| = 0.6$ to 0.65.

The mapping between the saturation analysis in $|\sigma_c|$ quantiles (Paper 1) to $|\delta n_H/n_H|$ reveals the following.

1. The minimum average $|\delta n_H/n_H|$ across $|\sigma_c|$ occurs in the most Alfvénic wind.
2. At the fastest speeds, the largest compressibility is in the least Alfvénic wind.
3. The compressibility in the most Alfvénic wind is independent of speed.
4. The compressibility varies with A_{He} across all $|\sigma_c|$ quantiles and reaches a local minimum at $A_{He} \gtrsim A_s$.
5. As with v_{sw}, the range of $|\delta n_H/n_H|$ is largest at the largest A_{He}. However, the maximum $|\delta n_H/n_H|$ in the fastest speeds is approximately twice as large as the maximum $|\delta n_H/n_H|$ in the largest A_{He}, suggesting that there is a narrower range of $|\delta n_H/n_H|$ within each $|\sigma_c|$ quantile at any v_{sw} than at any A_{He}.

From these observations, we infer that the transition from slow to fast solar wind at 1 AU is dominated by incompressible solar wind and that compressive fluctuations may lead to large variations in observations of fast wind.

In short, the empirical functions derived to map between $|\delta n_H/n_H|$ and $|\sigma_c|$ using saturation points reveals that the anti-correlation between $|\sigma_c|$ and $|\delta n_H/n_H|$ is absent in slow or helium-poor solar wind. As v_{sw} or A_{He} increase, the expected anti-correlation is recovered and it is most prominent in fast or helium-rich wind. These observations further support the inference there is not a unique mapping from a given v_{sw} to compressible, non-Alfvénic solar wind or incompressible, Alfvénic solar wind.

The mappings between saturation points as a function of $|\delta n_H/n_H|$ and $|\sigma_c|$ also reveals the dominant value of the other quantity. Across all $|\delta n_H/n_H|$ quantiles, only incompressible solar wind has a $|\sigma_c| \geq 0.6$, which is the $|\sigma_c|$ contour in Figure 6 at which we observe the saturation points derived in Paper 1, and the typical cross helicity is larger when $|\delta n_H/n_H|$ is mapped to $|\sigma_c|$ using A_s than when using v_s. The saturation points for compressible solar wind map to non-Alfvénic $|\sigma_c| < 0.6$. Across all $|\sigma_c|$ quantiles, $|\delta n_H/n_H|$ does not exceed 0.15, the largest incompressible threshold derived above. In particular, the dominant $|\delta n_H/n_H|$ across $|\sigma_c|$ is < 0.1 in Alfvénic solar wind. The $|\delta n_H/n_H|$ derived in each $|\sigma_c|$ quantile does not exceed 0.11 using A_s and does not exceed 0.132 using $|\sigma_c|$. These observations suggest that the enhanced $A_{He} > A_s$ subsets in Figure 15 and the enhanced $v_{sw} > v_s$ regions in Figure 16 do show that averaging in $|\delta n_H/n_H|$ quantiles or $|\sigma_c|$ quantiles does select for a wide range of values in the other quantity, impacting our determination of the saturation points and fits. Given the observations in Figures 2, 4 and 5, we infer that the saturation point is highly sensitive to both $|\sigma_c|$ and $|\delta n_H/n_H|$ and neglecting either leaves the analysis sensitive to a confounding variable. We also infer that aggregating solar wind observations without considering both the compressibility and the cross helicity mixes compressive and Alfvénic fluctuations, creating the apparent paradox in Sections 3.1 and 3.2.

5. CONCLUSION

Paper 1 shows that the solar wind can be separated into fast and slow based on the gradients of the helium abundance with solar wind speed, $\nabla_{v_{sw}} A_{He}$. This gradient changes at the saturation speed (v_s), which has a characteristic saturation abundance (A_s). Observations of this transition between slow and fast wind depends on $|\sigma_c|$. Paper 1 suggests that this transition can be used to classify classify solar wind by the magnetic topology of its source region using the $(|\sigma_c|, A_{He})$-plane. Paper 1 also infers that the minimum v_{sw} from source regions with continuously open magnetic topologies is slower than the maximum speed of solar wind originating in intermittently open source regions, which are sometimes referred to as "closed". This observation is consistent with Alfvénic slow wind as the low speed extension of solar wind that would otherwise be categorized as fast (D'Amicis & Bruno 2015; Wang 1994; Wang & Ko 2019; Panasenco et al. 2019, 2020; Panasenco & Velli 2013; Panasenco et al. 2019). However, Paper 1 shows that the gradient of A_{He} with v_{sw} at speeds $v_{sw} > v_s$ increase with decreasing $|\sigma_c|$. Figure 25 shows that this enhancement in A_{He} at fast speeds leads to a helium abundance far in excess of 50% the photospheric value, which is a consistent upper bound on A_{He} across the solar cycle (Alterman et al. 2025).

Analyzing A_{He} as a function of v_{sw} and $|\delta n_H/n_H|$ and comparing these results to the analysis in Paper 1 of A_{He} as a function of v_{sw} and $|\sigma_c|$, we have shown that the dependence of $\nabla_{v_{sw}} A_{He}$ on $|\sigma_c|$ at speeds $v_{sw} > v_s$ is due to the presence of compressive fluctuations in Alfvénic solar wind with high ($v_{sw} > v_s$) speeds. We have also shown that there exists two subsets of solar wind with enhanced $A_{He} > A_s$. In the Alfvénic subset, A_{He} does not vary. In the compressible subset, A_{He} varies by up to 80% in excess of the mean value. The average v_{sw} in this compressible subset is less variable than A_{He} in the Alfvénic subset. Comparing these two subsets of observations to the source region identification in Paper 1, we have shown that the incompressible subset likely corresponds to solar wind from magnetically open sources, but the compressible subset likely originated in

neither open nor closed source regions. This does not exclude that these compressive fluctuations are generated in transit.

Visualizing the range of speeds over which $\nabla_{v_{\rm sw}} A_{\rm He}$ changes in the compressible subset ($v_{\delta n'}$) on the distribution of speeds observed during solar minima at 1 AU shows the significance of compressible fluctuations on the separation of observations from open and closed sources. In particular, $v_{\delta n'}$ falls within the range of *ad hoc* speeds typically used to separate fast and slow wind. This range of speeds (v_{IP}) corresponds to wave-poor solar wind from continuously open source regions in which the energy in the Alfvénic fluctuations is reduced in comparison to typical fast wind (Alterman 2025) and is likely analogous to the Alfvénic slow wind (Marsch et al. 1981; D'Amicis et al. 2011). Given the enhancement of $A_{\rm He} > A_s$ due to compressive fluctuations in non-Alfvénic wind occurs at speeds $v_{\rm sw} > v_s$, this suggests that solar wind with compressive fluctuations from neither open nor closed sources is significant at these intermediate speeds.

The mappings between saturation points as a function of $|\delta n_{\rm H}/n_{\rm H}|$ and $|\sigma_c|$ reveals the dominant value of the other quantity. Across all $|\delta n_{\rm H}/n_{\rm H}|$ quantiles, only incompressible solar wind has a $|\sigma_c| \geq 0.6$, which is the $|\sigma_c|$ contour in Figure 6 at which we observe the saturation points derived in Paper 1, and the typical cross helicity is larger when $|\delta n_{\rm H}/n_{\rm H}|$ is mapped to $|\sigma_c|$ using A_s than when using v_s. The saturation points for compressible solar wind map to non-Alfvénic $|\sigma_c| < 0.6$. Across all $|\sigma_c|$ quantiles, $|\delta n_{\rm H}/n_{\rm H}|$ does not exceed 0.15, the largest incompressible threshold derived above. In particular, the dominant $|\delta n_{\rm H}/n_{\rm H}|$ across $|\sigma_c|$ is < 0.1 in Alfvénic solar wind. The $|\delta n_{\rm H}/n_{\rm H}|$ derived in each $|\sigma_c|$ quantile does not exceed 0.11 using A_s and does not exceed 0.132 using $|\sigma_c|$. These observations suggest that the enhanced $A_{\rm He} > A_s$ subsets in Figure 15 and the enhanced $v_{\rm sw} > v_s$ regions in Figure 16 do show that averaging in $|\delta n_{\rm H}/n_{\rm H}|$ quantiles or $|\sigma_c|$ quantiles selects for a wide range of values in the other quantity, impacting our determination of the saturation points and fits. Given the observations in Figures 2, 4 and 5, we infer that the saturation point is highly sensitive to both $|\sigma_c|$ and $|\delta n_{\rm H}/n_{\rm H}|$ and neglecting either leaves the analysis sensitive to a confounding variable.

From these observations, we conclude that a given $v_{\rm sw}$ does not uniquely map to either Alfvénic, incompressible or non-Alfvénic, compressible solar wind. Rather, the presence of enhanced compressive fluctuations across $v_{\rm sw}$ obscures the transition between fast and slow wind in our observations and confounds the mapping from fast/slow wind to open/closed source regions. We further conclude that the hydrogen compressibility is essential for characterizing and possibly regulating the solar wind helium abundance. This inference may be consistent with the role of pressure balanced structures (PBS), periodic density structures (PDS), or slow modes in the solar wind, all of which may also be related to solar wind source regions. Future work will determine how significant the role of transients is in this characterization of the role of compressibility in the solar wind and its relationship to the helium abundance. Combined with Paper 1, this work also suggests that a combination of $A_{\rm He}$, $|\sigma_c|$, and $|\delta n_{\rm H}/n_{\rm H}|$ may be sufficient to map the solar wind to its source region when composition observations are unavailable.

ACKNOWLEDGMENTS

The authors thank the referee for their helpful and supportive feedback. The authors are grateful to Mihailo M. Martinović and Kristopher G. Klein for valuable discussions. The authors also thank Nicholeen Viall and Brent Randol for useful discussions about periodic density structures. The authors thank Yogesh for discussions about the typical helium abundance in SIRs. Wind Faraday cup data are obtained from CDAWeb. The authors acknowledge Justin C. Kasper for the development and Michael L. Stevens for the delivery of this data product. B.L.A. is funded by grants 80NSSC22K0645 (LWS/TM) and 80NSSC22K1011 (LWS) along with Parker Solar Probe and Solar Orbiter funding at NASA Goddard Space Flight Center.

Software: IPython (Perez & Granger 2007), Jupyter (Kluyver et al. 2016), Matplotlib (Hunter 2007), Numpy (Harris et al. 2020; van der Walt et al. 2011), SciPy (Jones et al. 2001; Virtanen et al. 2020), Pandas (Mckinney 2010; McKinney 2011; Mckinney 2013), Python (Millman & Aivazis 2011; Oliphant 2007), Mathematica (Wolfram Research, Inc. 2024)

REFERENCES

Abbo, L., Ofman, L., Antiochos, S. K., et al. 2016, Space Science Reviews, 201, 55, doi: 10.1007/s11214-016-0264-1

Adhikari, L., Zank, G. P., Zhao, L. L., et al. 2020, The Astrophysical Journal Supplement Series, 246, 38, doi: 10.3847/1538-4365/ab5852

Aellig, M. R., Lazarus, A. J., & Steinberg, J. T. 2001, Geophysical Research Letters, 28, 2767, doi: 10.1029/2000GL012771

Alterman, B. 2025, Astrophysical Journal Letters

Alterman, B. L., & D'Amicis, R. 2025a, Astrophysical Journal Letters (in prep)

—. 2025b, in prep

Alterman, B. L., & D'Amicis, R. 2025, The Astrophysical Journal Letters, 982, L40, doi: 10.3847/2041-8213/adb48e

Alterman, B. L., & Kasper, J. C. 2019, The Astrophysical Journal, 879, L6, doi: 10.3847/2041-8213/ab2391

Alterman, B. L., Kasper, J. C., Leamon, R. J., & McIntosh, S. W. 2021, Solar Physics, 296, 67, doi: 10.1007/s11207-021-01801-9

Alterman, B. L., Kasper, J. C., Stevens, M., & Koval, A. 2018, The Astrophysical Journal, 864, 112, doi: 10.3847/1538-4357/aad23f

Alterman, B. L., Rivera, Y. J., Raines, J. M., Lepri, S. T., & D'Amicis, R. 2025, Astronomy & Astrophysics (in review)

Alterman, B. L., Y. J. Rivera, Lepri, S. T., & Raines, J. M. 2024, Astronomy & Astrophysics, doi: 10.1051/0004-6361/202451550

Antiochos, S. K., Mikic, Z., Titov, V. S., Lionello, R., & Linker, J. A. 2011, The Astrophysical Journal, 112, doi: 10.1088/0004-637X/731/2/112

Antonucci, E., Abbo, L., & Dodero, M. A. 2005, Astronomy & Astrophysics, 435, 699, doi: 10.1051/0004-6361:20047126

Asplund, M., Amarsi, A. M., & Grevesse, N. 2021, Astronomy & Astrophysics, 653, A141, doi: 10.1051/0004-6361/202140445

Berger, L., Wimmer-Schweingruber, R. F., & Gloeckler, G. 2011, Physical Review Letters, 106, 151103, doi: 10.1103/PhysRevLett.106.151103

Brooks, D. H., Ugarte-Urra, I., & Warren, H. P. 2015, Nature Communications, 6, doi: 10.1038/ncomms6947

Bruno, R., & Carbone, V. 2013, Living Reviews in Solar Physics, 10, 1, doi: 10.12942/lrsp-2013-2

Bruno, R., Carbone, V., Veltri, P., Pietropaolo, E., & Bavassano, B. 2001, Planetary and Space Science, 49, 1201, doi: 10.1016/S0032-0633(01)00061-7

Chitta, L. P., Huang, Z., D'Amicis, R., et al. 2025, Astronomy & Astrophysics, 694, A71, doi: 10.1051/0004-6361/202452737

Crooker, N. U., Antiochos, S. K., Zhao, X., & Neugebauer, M. 2012, Journal of Geophysical Research: Space Physics, 117, n/a, doi: 10.1029/2011JA017236

Cuesta, M. E., Chhiber, R., Fu, X., et al. 2023, The Astrophysical Journal Letters, 949, L19, doi: 10.3847/2041-8213/acd4c2

D'Amicis, R., & Bruno, R. 2015, Astrophysical Journal, 805, 1, doi: 10.1088/0004-637X/805/1/84

D'Amicis, R., Bruno, R., & Matteini, L. 2016, AIP Conference Proceedings, 1720, doi: 10.1063/1.4943813

D'Amicis, R., Matteini, L., & Bruno, R. 2018, Monthly Notices of the Royal Astronomical Society, 14, 1, doi: 10.1093/mnras/sty3329

D'Amicis, R., Alielden, K., Perrone, D., et al. 2021a, Astronomy & Astrophysics, 654, A111, doi: 10.1051/0004-6361/202140600

D'Amicis, R., Bruno, R., & Bavassano, B. 2011, Journal of Atmospheric and Solar-Terrestrial Physics, 73, 653, doi: 10.1016/j.jastp.2011.01.012

D'Amicis, R., Perrone, D., Bruno, R., & Velli, M. 2021b, Journal of Geophysical Research: Space Physics, 126, doi: 10.1029/2020JA028996

D'Amicis, R., Perrone, D., Velli, M., et al. 2022, Universe, 8, 352, doi: 10.3390/universe8070352

Elsasser, W. M. 1950, Physical Review, 79, 183, doi: 10.1103/PhysRev.79.183

Endeve, E., Lie-Svendsen, O., Hansteen, V. H., & Leer, E. 2005, The Astrophysical Journal, 624, 402, doi: 10.1086/428938

Fisk, L. A., Zurbuchen, T. H., & Schwadron, N. A. 1999, The Astrophysical Journal, 521, 868, doi: 10.1086/307556

Fu, H., Li, B., Li, X., et al. 2015, Solar Physics, 290, 1399, doi: 10.1007/s11207-015-0689-9

Fu, H., Madjarska, M. S., Li, B., Xia, L., & Huang, Z. 2018, Monthly Notices of the Royal Astronomical Society, 478, 1884, doi: 10.1093/mnras/sty1211

Fu, H., Madjarska, M. S., Xia, L., et al. 2017, The Astrophysical Journal, 836, 169, doi: 10.3847/1538-4357/aa5cba

Geiss, J., Gloeckler, G., & von Steiger, R. 1995a, Space Science Reviews, 72, 49

Geiss, J., Gloeckler, G., Von Steiger, R., et al. 1995b, Science, 268, 1033, doi: 10.1126/science.7754380

Good, S. W., Hatakka, L. M., Ala-Lahti, M., et al. 2022, Monthly Notices of the Royal Astronomical Society, 514, 2425, doi: 10.1093/mnras/stac1388

Grappin, R., Velli, M., & Mangeney, A. 1991, Annales Geophysicae, 9, 416

Hansteen, V. H., Leer, E., & Holzer, T. E. 1997, The Astrophysical Journal, 482, 498, doi: 10.1086/304111

Harris, C. R., Millman, K. J., van der Walt, S. J., et al. 2020, Nature, 585, 357, doi: 10.1038/s41586-020-2649-2

Hollweg, J. V., Verscharen, D., & Chandran, B. D. G. 2014, The Astrophysical Journal, 788, 35, doi: 10.1088/0004-637X/788/1/35

Hunter, J. D. 2007, Computing in Science & Engineering, 9, 90, doi: 10.1109/MCSE.2007.55

Jones, E., Oliphant, T. E., Peterson, P., & others. 2001, {SciPy}: Open source scientific tools for {Python}. http://www.scipy.org/

Kasper, J. C., Lazarus, A. J., & Gary, S. P. 2008, Physical Review Letters, 101, 261103, doi: 10.1103/PhysRevLett.101.261103

Kasper, J. C., Lazarus, A. J., Steinberg, J. T., Ogilvie, K. W., & Szabo, A. 2006, Journal of Geophysical Research, 111, A03105, doi: 10.1029/2005JA011442

Kasper, J. C., Stevens, M., Lazarus, A. J., Steinberg, J. T., & Ogilvie, K. W. 2007, The Astrophysical Journal, 660, 901, doi: 10.1086/510842

Kasper, J. C., Klein, K. G., Weber, T., et al. 2017, The Astrophysical Journal, 849, 126, doi: 10.3847/1538-4357/aa84b1

Kepko, L., Viall, N. M., & DiMatteo, S. 2024, Journal of Geophysical Research: Space Physics, 129, e2023JA031403, doi: 10.1029/2023JA031403

Khokhlachev, A. A., Yermolaev, Y. I., Lodkina, I. G., Riazantseva, M. O., & Rakhmanova, L. S. 2022, Cosmic Research, 60, 67, doi: 10.1134/S0010952522020046

Klein, K. G., Verniero, J. L., Alterman, B. L., et al. 2021, The Astrophysical Journal, 909, 7, doi: 10.3847/1538-4357/abd7a0

Kluyver, T., Ragan-Kelley, B., Pérez, F., et al. 2016, in Positioning and Power in Academic Publishing: Players, Agents and Agendas, ed. F. Loizides & B. Schmidt (IOS Press), 87–90

Koval, A., & Szabo, A. 2013, in AIP Conference Proceedings, Vol. 1539, 211–214, doi: 10.1063/1.4811025

Lepping, R. P., Acũna, M. H., Burlaga, L. F., et al. 1995, Space Science Reviews, 71, 207, doi: 10.1007/BF00751330

Lepri, S. T., Landi, E., & Zurbuchen, T. H. 2013, The Astrophysical Journal, 768, 94, doi: 10.1088/0004-637X/768/1/94

Lie-Svendsen, O., Leer, E., & Hansteen, V. H. 2001, Journal of Geophysical Research: Space Physics, 106, 8217, doi: 10.1029/2000JA000409

Lie-Svendsen, O., Hansteen, V. H., & Leer, E. 2003, The Astrophysical Journal, 596, 621, doi: 10.1086/377640

Lie-Svendsen, O., Hansteen, V. H., Leer, E., & Holzer, T. E. 2002, The Astrophysical Journal, 566, 562, doi: 10.1086/337990

Liu, M., Issautier, K., Meyer-Vernet, N., et al. 2021, Astronomy & Astrophysics, 650, A14, doi: 10.1051/0004-6361/202039615

Marsch, E., Mühlhäuser, K.-H., Rosenbauer, H., Schwenn, R., & Denskat, K. U. 1981, Journal of Geophysical Research, 86, 9199, doi: 10.1029/JA086iA11p09199

Marsch, E., & Tu, C. 1990, Journal of Geophysical Research: Space Physics, 95, 11945, doi: 10.1029/JA095iA08p11945

Matteini, L., Horbury, T. S., Pantellini, F., Velli, M., & Schwartz, S. J. 2015, The Astrophysical Journal, 802, 11, doi: 10.1088/0004-637X/802/1/11

Mckinney, W. 2010, in Proceedings of the 9th Python in Science Conference, ed. S. van der Walt & J. Millman, 51 – 56

McKinney, W. 2011, Python for High Performance and Scientific Computing, 1

Mckinney, W. 2013, Python for Data Analysis (O'Reilly), doi: 10.1145/1985441.1985476

McManus, M. D., Bowen, T. A., Mallet, A., et al. 2020, The Astrophysical Journal Supplement Series, 246, 67, doi: 10.3847/1538-4365/ab6dce

Millman, K. J., & Aivazis, M. 2011, Computing in Science & Engineering, 13, 9, doi: 10.1109/MCSE.2011.36

Ogilvie, K. W., Chornay, D. J., Fritzenreiter, R. J., et al. 1995, Space Science Reviews, 71, 55, doi: 10.1007/BF00751326

Oliphant, T. E. 2007, Computing in Science & Engineering, 9, 10, doi: 10.1109/MCSE.2007.58

Panasenco, O., & Velli, M. 2013, in Solar Wind 13, Big Island, Hawaii, 50–53, doi: 10.1063/1.4810987

Panasenco, O., Velli, M., & Panasenco, A. 2019, The Astrophysical Journal, 873, 25, doi: 10.3847/1538-4357/ab017c

Panasenco, O., Velli, M., D'Amicis, R., et al. 2020, The Astrophysical Journal Supplement Series, 246, 54, doi: 10.3847/1538-4365/ab61f4

Perez, F., & Granger, B. E. 2007, Computing in Science & Engineering, 9, 21, doi: 10.1109/MCSE.2007.53

Phillips, J. L., Balogh, A., Bame, S. J., et al. 1994, Geophysical Research Letters, 21, 1105, doi: 10.1029/94GL01065

Pilleri, P., Reisenfeld, D. B., Zurbuchen, T. H., et al. 2015, The Astrophysical Journal, 812, 1, doi: 10.1088/0004-637X/812/1/1

Rivera, Y. J., Badman, S. T., Stevens, M. L., et al. 2024, Science, 385, 962, doi: 10.1126/science.adk6953

Rivera, Y. J., Badman, S. T., Verniero, J. L., et al. 2025, The Astrophysical Journal, 980, 70, doi: 10.3847/1538-4357/ada699

Savitzky, A., & Golay, M. J. E. 1964, Analytical Chemistry, 36, 1627, doi: 10.1021/ac60214a047
Schwenn, R. 2006, Space Science Reviews, 124, 51, doi: 10.1007/s11214-006-9099-5
Scolini, C., Lugaz, N., Winslow, R. M., et al. 2024, The Astrophysical Journal, 961, 135, doi: 10.3847/1538-4357/ad0ed1
Song, H., Cheng, X., Li, L., Zhang, J., & Chen, Y. 2022, The Astrophysical Journal, 925, 137, doi: 10.3847/1538-4357/ac3bbf
Stakhiv, M. O., Lepri, S. T., Landi, E., Tracy, P. J., & Zurbuchen, T. H. 2016, The Astrophysical Journal, 829, 117, doi: 10.3847/0004-637X/829/2/117
Starkey, M. J., Fuselier, S. A., & Dayeh, M. A. 2024, Journal of Geophysical Research: Space Physics, 129, e2024JA033099, doi: 10.1029/2024JA033099
Steinier, J., Termonia, Y., & Deltour, J. 1972, Analytical Chemistry, 44, 1906, doi: 10.1021/ac60319a045
Subramanian, S., Madjarska, M. S., & Doyle, J. G. 2010, Astronomy and Astrophysics, 516, A50, doi: 10.1051/0004-6361/200913624
Tracy, P. J., Kasper, J. C., Raines, J. M., et al. 2016, Physical Review Letters, 255101, 255101, doi: 10.1103/PhysRevLett.116.255101
Tu, C.-Y., & Marsch, E. 1994, Journal of Geophysical Research: Space Physics, 99, 21481, doi: 10.1029/94JA00843
Tu, C. Y., & Marsch, E. 1995, Space Science Reviews, 73, 1, doi: 10.1007/BF00748891
Tu, C.-Y., Marsch, E., & Thieme, K. M. 1989, Journal of Geophysical Research, 94, 11739, doi: 10.1029/ja094ia09p11739
van der Walt, S., Colbert, S. C., & Varoquaux, G. 2011, Computing in Science & Engineering, 13, 22, doi: 10.1109/MCSE.2011.37
Vasquez, B. J., & Hollweg, J. V. 1999, Journal of Geophysical Research: Space Physics, 104, 4681, doi: 10.1029/1998JA900090
Verniero, J. L., Larson, D. E., Livi, R., et al. 2020, The Astrophysical Journal Supplement Series, 248, 5, doi: 10.3847/1538-4365/ab86af
Verniero, J. L., Chandran, B. D. G., Larson, D. E., et al. 2022, The Astrophysical Journal, 924, 112, doi: 10.3847/1538-4357/ac36d5
Verscharen, D., Chandran, B. D. G., Klein, K. G., & Quataert, E. 2016, The Astrophysical Journal, 831, 128, doi: 10.3847/0004-637X/831/2/128
Verscharen, D., Chen, C. H. K., & Wicks, R. T. 2017, The Astrophysical Journal, 840, 106, doi: 10.3847/1538-4357/aa6a56
Viall, N. M., Spence, H. E., & Kasper, J. C. 2009, Geophysical Research Letters, 36, 1, doi: 10.1029/2009GL041191
Viall, N. M., & Vourlidas, A. 2015, The Astrophysical Journal, 807, 176, doi: 10.1088/0004-637X/807/2/176
Virtanen, P., Gommers, R., Oliphant, T. E., et al. 2020, Nature Methods, 17, 261, doi: 10.1038/s41592-019-0686-2
von Steiger, R., Schwadron, N. A., Fisk, L. A., et al. 2000, Journal of Geophysical Research: Space Physics, 105, 27217, doi: 10.1029/1999JA000358
Wang, Y.-M. 1994, The Astrophysical Journal, 437, L67, doi: 10.1086/187684
Wang, Y.-M., & Ko, Y.-K. 2019, The Astrophysical Journal, 880, 146, doi: 10.3847/1538-4357/ab2add
Webb, D. F., & Howard, T. A. 2012, Living Reviews in Solar Physics, 9, doi: 10.12942/lrsp-2012-3
Wolfram Research, Inc. 2024, Champaign, Illinois: Wolfram Research, Inc. https://www.wolfram.com/mathematica
Woodham, L. D., Wicks, R. T., Verscharen, D., & Owen, C. J. 2018, The Astrophysical Journal, 856, 49, doi: 10.3847/1538-4357/aab03d
Xu, F., & Borovsky, J. 2015, Journal of Geophysical Research: Space Physics, 120, 70, doi: 10.1002/2014JA020412
Yardley, S. L., Brooks, D. H., D'Amicis, R., et al. 2024, Nature Astronomy, doi: 10.1038/s41550-024-02278-9
Yogesh, Chakrabarty, D., & Srivastava, N. 2021, Monthly Notices of the Royal Astronomical Society: Letters, 503, L17, doi: 10.1093/mnrasl/slab016
—. 2022, Monthly Notices of the Royal Astronomical Society: Letters, 111, 106, doi: 10.1093/mnrasl/slac044
—. 2023, Monthly Notices of the Royal Astronomical Society, 526, L13, doi: 10.1093/mnrasl/slad112
Zank, G. P., & Matthaeus, W. H. 1992, Journal of Geophysical Research: Space Physics, 97, 17189, doi: 10.1029/92JA01734
Zhao, L., Landi, E., Lepri, S. T., & Carpenter, D. 2022, Universe, 8, 393, doi: 10.3390/universe8080393
Zhao, L., Landi, E., Lepri, S. T., et al. 2017, The Astrophysical Journal, 846, 135, doi: 10.3847/1538-4357/aa850c
Zhu, X., Verscharen, D., He, J., Maruca, B. A., & Owen, C. J. 2023, The Astrophysical Journal, 956, 66, doi: 10.3847/1538-4357/aced03
Zurbuchen, T. H., Weberg, M., Von Steiger, R., et al. 2016, The Astrophysical Journal, 826, 10, doi: 10.3847/0004-637X/826/1/10
Ďurovcová, T., Němeček, Z., & Šafránková, J. 2019a, The Astrophysical Journal, 873, 24, doi: 10.3847/1538-4357/ab01c8

Ďurovcová, T., Šafránková, J., & Němeček, Z. 2019b, Solar Physics, 294, 97, doi: 10.1007/s11207-019-1490-y